

## RESEARCH ARTICLE

# Studies of relative contributions of internal gravity waves and 2-D turbulence to tropospheric and lower-stratospheric temporal wind spectra measured by a network of VHF windprofiler radars using a decade-long data set in Canada

Wayne K. Hocking<sup>1</sup>  | Sergio Dempsey<sup>1</sup> | Mel Wright<sup>1,2</sup> | Peter Taylor<sup>3</sup> | Frédéric Fabry<sup>4</sup>

<sup>1</sup>Department of Physics and Astronomy, University of Western Ontario, London, Ontario Canada

<sup>2</sup>Knutsford Academy, Knutsford, UK

<sup>3</sup>Department of Earth & Space Science & Engineering, York University, Toronto, Ontario Canada

<sup>4</sup>Atmospheric and Oceanic Sciences and School of Environment, McGill University, Montreal, Quebec Canada

## Correspondence

W. K. Hocking, Department of Physics and Astronomy, University of Western Ontario, London, N6A 3K7, ON, Canada.  
Email: whocking@uwo.ca

## Funding information

Natural Sciences and Engineering Research Council of Canada, Grant/Award Number: RGPIN-2018-04242

## Abstract

Tropospheric and lower-stratospheric motions at mesoscales and larger are a mixture of waves and two-dimensional (2-D) turbulence. Determining their relative importance is necessary, since waves are capable of coordinated systematic momentum transport accompanying the wave propagation, and associated wind forcing, in ways that 2-D turbulence is not. This can impact weather forecasting. Using a network of ten windprofiler radars in eastern Ontario and western Quebec in Canada, plus an additional one in the Arctic, the relative roles of internal gravity (buoyancy) waves and two-dimensional turbulence are examined at temporal scales from about 3–4 hrs to several tens of hours (horizontal spatial scales of typically one or two hundred kilometres to a few thousand kilometres), with the purpose of investigating the respective roles of these two distinct characteristic fluid motions as functions of location, season and year. The emphasis is on studies of spectral slope variability, rather than absolute spectral magnitudes, giving a perspective not previously substantially presented. In particular, we have found a frequency band in which gravity-wave Doppler shifting produces distinctly different spectral slopes than those predicted for 2-D turbulence, and these differences are employed to distinguish the flow fields. The network used (excluding the Arctic site) covers an area of  $\sim 10^6$  km<sup>2</sup> and includes a variety of different terrains. Radial velocities have been recorded on time scales of minutes for data lengths covering durations of up to 12 years. Altitude coverage is from 1 km to typically 14 km, at 500 m resolution. Results suggest a region from  $\sim 2$  to  $\sim 5$  km altitude (deeper for some radars) where waves are weaker and 2-D turbulence appears to be generally more significant, but where occasional bursts of gravity-wave activity can occur, while above typically 6–8 km, gravity waves increase in significance. There are distinct site-to-site variations.

## KEYWORDS

2-D turbulence, data-compensated discrete Fourier transform, Doppler shifting, geographic variability, internal gravity waves, profilers, statistical significance, temporal spectrum, universal spectrum

This is an open access article under the terms of the Creative Commons Attribution License, which permits use, distribution and reproduction in any medium, provided the original work is properly cited.

© 2021 The Authors. *Quarterly Journal of the Royal Meteorological Society* published by John Wiley & Sons Ltd on behalf of the Royal Meteorological Society.

## 1 | INTRODUCTION

There has been a long-standing debate about the relative contributions of internal gravity (buoyancy) waves and 2-D turbulence in the lower atmosphere in the period range from a few minutes to several days. While the importance of waves in the stratosphere and mesosphere is well established, with strong dominance by planetary waves in regard to stratospheric motions, and very strong internal gravity wave (IGW) activity in the mesosphere (e.g., Lindzen, 1981; Fritts and Alexander, 2003; Thayaparan *et al.*, 1995, and references there-in; Hocking *et al.*, 2016), arguments persist as to the relative importance of IGWs in the troposphere and lower stratosphere. Some authors consider them to be important, while others consider them as largely “noise” (e.g., see discussions in Pisoft *et al.*, 2018; Minamihara *et al.*, 2018; and Sutherland, 2010, for various views). The general exponential growth of gravity wave amplitudes with increasing height means that an increase in the dominance of these waves is to be expected at higher altitudes, while perhaps (though not necessarily) 2-D turbulence might be more important at lower altitudes. Few studies have been dedicated to a quantitative and extensive evaluation of these different points of view. Some studies of wave magnitudes and variances (e.g., Nastrom *et al.*, 1987, using GASP data) have been interpreted as support for a gravity-wave theory. That work used the fact that the log of power spectral densities were linear as a function of the log of the wavenumber, with slopes on the order of  $-5/3$  to  $-2$ , which is indeed supportive of gravity wave models. However, while such slopes do support gravity wave theory, these slopes are not exclusive to that proposal, and could possibly be attributed to turbulence (e.g., Lilly, 1983; 1989; Lindborg, 1999 (hereafter L99), Tung and Orlando, 2003 (hereafter TO03), and references there-in).

It is important to note that it is not possible to determine the relative roles of waves versus non-wave-like activity by simple pattern recognition; certainly strong individual waves can appear as distinct wave-like patterns in clouds, for example, but a sufficient number of weaker waves can appear just like a turbulent regime. Some more recent papers make an implicit assumption that the majority of the oscillations with periods between a few minutes and a significant fraction of a day, and horizontal wavelengths from tens to many hundreds of kilometres, are indeed gravity waves. For example, Minamihara *et al.* (2018) have shown spectra of oscillations that they associate with gravity wave activity in Antarctica, and other papers have measured momentum fluxes in the stratosphere and upper troposphere (e.g., Geller *et al.*, 2013; Fritts *et al.*, 2016). In the latter cases, the non-zero values deduced for momentum fluxes are an

indication that the oscillations observed must be due to gravity waves, but those studies were in the main stratospheric and above. Furthermore, Fritts *et al.* (2016) specifically sought out gravity wave “hot-spots” for their studies. The article by Minamihara *et al.* (2018) contains a list of recent references pertaining to gravity wave studies in the troposphere and lower stratosphere. The question that remains is: what is the lowest altitude above which gravity wave activity can generally be considered to be stronger in its impact on the atmosphere than 2-D turbulence?

Before proceeding, it is appropriate that the distinctions between waves and 2-D turbulence are understood. Waves are well understood by most readers: the most important feature of waves from our perspective is that they have a dispersion relation that links the period, wavelength and wave speed. They are also capable of transporting energy and momentum fluxes large distances. In regard to 2-D turbulence, we consider it as comprising “eddies” of different sizes, stratified in layers, which are two-dimensional in nature (no altitude coordinate). In the idealized case, they are statistically stationary in time (no “period” can be associated with them), and comprise different horizontal scales which have (nominally) repeatable spectral behaviour as a function of spatial wavenumber. They have no dispersion relation, and cannot transport momentum or energy in the way that a wave can. In our case, the 2-D turbulence that is observed covers scales from quasi-geostrophic (Q-G) turbulence down to mesoscales and smaller. A variety of mechanisms have been proposed to create these eddies, including down-scale enstrophy transport and up-scale energy transport. According to some authors, baroclinic instability and Ekman damping are important. Down-scale energy transport, through short synoptic eddies and on to mesoscales, is also considered in some models. Relevant theories of creation are discussed by L99, and TO03.

One feature that will be assumed throughout this work is that both the IGW spectrum and the 2-D turbulence spectrum (which we take to include Q-G turbulence) are isotropic in the horizontal plane. With regard to IGWs, it is assumed that waves are equally likely to be propagating in any horizontal direction: while there may be local variations in this, our data span more than 10 years of data, at 11 different sites, so such isotropy should be a reasonable long-term assumption. With regard to 2-D turbulence, isotropy means that any individual “snapshot” of the eddy structure will look statistically similar if rotated by an arbitrary angle in the horizontal plane. There will be no long-term tendency for eddies to appear stretched in any preferred direction, for example, or for any one direction to show greater intensity of fluctuation than any other (after sufficient averaging). This will be verified later in the text by comparing data recorded in orthogonal directions,

and will be shown to be generally true irrespective of the nature of the oscillations (IGWs or 2-D turbulence).

A new approach is needed to discriminate more definitively between gravity waves and 2-D turbulence, since the estimated mean slopes for 2-D turbulence and the intrinsic gravity wave spectra (i.e., the gravity wave spectra seen before Doppler effects are considered) are too similar in value to be used as a useful discriminator. Studies of momentum flux help, but in this article an alternative approach is demonstrated. The new method relies on the fact that *Doppler shifting* of wave-like events leads to profound differences in gravity wave and 2-D turbulence spectra, where such differences are not so apparent without Doppler shifting. Our procedure relies on modelling studies (introduced in Section 4) which reveal a frequency band in which real gravity wave spectra (i.e., Doppler-shifted rather than intrinsic spectra) and 2-D turbulence spectra do indeed show significantly different slopes. This band is close to the atmospheric inertial frequency, and our studies will be concentrated there. Importantly, in our investigations, regions known to have strong gravity wave activity (hot-spots) have not been sought out; rather, an area of the world has been chosen which can be considered topographically and geophysically quite “average”.

More specifically, the coherent nature of gravity waves will allow them to be Doppler shifted by the mean wind to varying degrees, resulting in changes in spectral slopes (as viewed by a stationary observer on the ground) under different wind conditions (Scheffler and Liu, 1985; 1986; Fritts and Van Zandt, 1987 [hereafter FVZ87]; Smith *et al.*, 1985; 1987), with particular spectral bands showing stronger Doppler-shifting effects. On the other hand, largely incoherent processes such as 2-D statistically stationary turbulence will, under equilibrium conditions and according to common theory (e.g., Gage, 1979; Lilly, 1983, L99, TO03), produce a well-defined wavenumber spectrum with no statistically significant localized wavenumber peaks or dips, and furthermore for radar studies the wavenumber spectrum will convert directly to a frequency spectrum via the Taylor frozen-in hypothesis (Taylor, 1938).

With regard to 2-D turbulence models, recent proposals have been presented by a variety of authors, including L99, TO03, Koshyk and Hamilton (2001) and Cho and Lindborg (2001). While differing in details, each proposes a similar form for the wavenumber spectrum, this being of the following form (L99, equation [71]):

$$E_1(k) = d_1 k^{-\gamma} + d_2 k^{-\xi}. \quad (1)$$

We will take the values determined by L99 as a reference for our work, viz.  $d_1 = 9.1 \times 10^{-4}$  and  $d_2 = 3.0 \times 10^{-10}$ ,

where  $k$  is expressed in rad/m (see fig. 1 in L99, upper label, but note that the lower axis is wrongly labelled in that article; it should be “wavelength [km]”). L99 used MOZAIC data (Marenco *et al.*, 1998) and showed that  $\gamma = 5/3$ ,  $\xi = 3$  for the fitting. However, we emphasize that the reasons for the two distinct slopes is still under discussion and has been receiving continuing attention. While no consensus has yet been reached, for the purposes of this article, our only requirement is that the model be based on acceptable physical foundations. TO03 gives a good overview of the various proposed models; there is general agreement that the dual power-law shown in Equation (1) is physically valid. We leave it to the reader to pursue these mechanisms if interested. It is also important to note that different data sets (e.g., MOZAIC (Marenco *et al.*, 1998), compared with Nastrom and Gage (1985) give slightly different values for  $d_1$  and  $d_2$ , but there is a significant level of universality across the different measurements, and variations in  $d_1$  and  $d_2$  between data sets are considered to be modest. TO03 (among others) discusses this in some detail. We will allow for such variations in our analyses.

If a sensor passes through the turbulent medium with speed  $\bar{u}$  (or equivalently the region passes by a fixed detector, such as a radar, with speed  $\bar{u}$ ), and the medium is assumed to be statistically stationary and homogeneous, then the measured angular frequency of a wavenumber  $k$  will be  $\omega = \bar{u}k$ . If the frequency spectrum is written as  $F_\omega(\omega)$ , then applying a standard 1-D Jacobian gives  $F_\omega(\omega) = E_1(k)(dk/d\omega) = E_1/\bar{u}$ . Hence,

$$F_\omega(\omega) = d_1 \bar{u}^{-(\gamma-1)} \omega^{-\gamma} + d_2 \bar{u}^{-(\xi-1)} \omega^{-\xi} \quad (2)$$

This will be the theoretical function against which data will be compared when testing for 2-D turbulence-like behaviour. Further commentary appears in Section 4.2.

In regard to gravity waves, changes in spectral slope are expected due to Doppler shifting, and FVZ87 have determined expressions for expected changes to the spectral form under different conditions of mean wind speed and wave phase speed. Comparisons of the predictions of L99 or TO03 with FVZ87 against our data will form the basis of this article.

On a related topic, there is also considerable debate about the relative roles of rotational (geostrophic) motion and divergent motions in flows on the scales under consideration. While in some senses this is a different issue when it comes to specific details, it is related to the present study: high-frequency gravity waves (with periods of less than a few hours) are primarily divergent, while waves with periods comparable to the inertial frequency, and 2-D turbulence, have strong rotational aspects. In this regard, Bühler *et al.* (2014) (hereafter BCF14) presented a method

to use data recorded along extended paths traced out by aircraft and ships to disentangle divergent and rotational aspects of 2-D motion. While of interest, there are various reasons why BCF14 is unsuitable for our radar studies. First, the BCF14 method applies to wavenumber spectra, and uses a Helmholtz decomposition, which is inherently a spatial-scale-dependent decomposition. It is not suitable to deal with our data. Furthermore, it relies on comparison of transverse and longitudinal spectra, and intercompares spectral amplitudes, whereas our method will be based on comparisons of spectral slopes after consideration of Doppler shifting. The interested reader is invited to view BCF14 as perhaps a complementary method, but we will not discuss it further herein. With these points in mind, we concentrate on utilizing our Doppler-based method, which directly utilizes radial velocities and so is better matched to the radar data.

Our approach, then, will be to search for evidence of variability in the spectral slopes of  $\log(\text{power density})$  versus  $\log(\text{frequency})$  in a critical frequency band close to the inertial frequency, as a function of time (on scales from months to years), altitude and geographic location, using a network of profiler radars in eastern Ontario and western Quebec in Canada. This radar network is referred to as the O-QNet (Ontario-Quebec NETWORK). An additional polar radar at  $80^\circ$  N is also used. In Section 2 the radar network is described. In Section 3, a broad overview of the method is presented, and special features of the O-QNet that have made this study possible are highlighted. In Section 4.1, the relevant basics of gravity wave theory are presented, and the primary parameters that will be studied are outlined, while pertinent properties pertaining to 2-D and Q-G turbulence are outlined in Section 4.2. In Section 5, specific details of the analysis will be discussed, and Section 6 will present results. The main body of the text is supported by Appendix A and Appendices S1, S2, S3 and S4; the latter gives further information of general interest about the radar network, presents some basic theory regarding IGWs that is of relevance to the article and shows some details about the statistical reliability of our results. Discussion and conclusions are presented as Sections 7 and 8.

## 2 | INSTRUMENTATION

In these studies, wind profilers have been used to analyse atmospheric motions over multiple sites, using time series with lengths spanning from 5 up to 12 years; the mean duration per site was 8 years. These radars use narrow radar beams pointing at different angles in the sky to determine along-bore radial velocity components of the wind, from which vector winds are generally determined.



**FIGURE 1** Map of the radars of the O-QNet. Radars are indicated by a cross (x)

General discussions about such radars are given in Hocking *et al.* (2016).

The locations of the O-QNet radars are shown in Figure 1; an additional polar radar exists at Eureka in Nunavut, Canada, in the Arctic ( $80^\circ$  N,  $85.9^\circ$  W), but is not shown on the map. The typical separation between neighbouring radars in the O-QNet was about 200 km, with some nearest neighbours as close as 100 km. There were 11 radars in all (including Eureka). The radars were installed in the period from 2002 to 2014, and typically one or two radars were built per year. Radars began operation as soon as commissioning was complete.

The O-QNet is discussed by Hocking *et al.*, 2007; 2009, and a demonstration of the data quality has been given by Taylor *et al.* (2016). Extensive comparisons of profiler winds against radiosonde winds have also been made, showing good agreement (e.g., see Hocking *et al.*, 2016). The quality of the data is also verified by the fact that winds from the O-QNet have been incorporated into CWINDE worldwide weather forecasts on an hourly basis for many years (Illingworth *et al.*, 2015).

Typical cross-sections (from Google Maps) across the O-QNet region are shown in Figure 2, revealing regions of flat land (near Harrow, Gananoque and Montreal), and more undulating and hilly regions nearer Negro Creek and Aumond (both these sites have ski resorts nearby, so have modest-sized hills). For reference, the highest point in Ontario is at Ishpatina Ridge, just north of Sudbury, being 693 m above sea level. There are no peaks in the region of the O-QNet over 1,000 m ASL (above sea level).



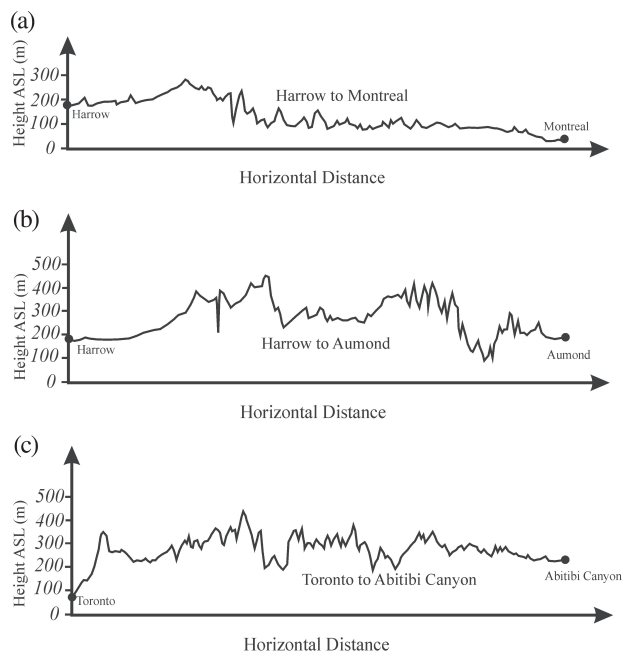


**FIGURE 2** Cross-sections of the terrain along approximately straight lines (following the nearest roadways) from (a) Harrow to Montreal, (b) Harrow to Aumond and (c) Toronto through Egbert and on to Abitibi canyon (adapted from Google Maps)

The taller hills tend to rise only a few hundred metres above the surrounding countryside.

The wind profiler radars each had five main beam directions (one vertical, and four off-vertical at azimuthal steps of  $90^\circ$ ), and each radar cycled between those beams on roughly a minute by minute basis throughout the year, with time intervals varying by  $\pm 10$  s depending on the recording mode. On each acquisition, radar spectra were generated and subject to various tests; acceptable spectra were then used to determine radial velocities. Acceptance rates at 2–5 km altitude were above 80%, with slightly reduced acceptance rates at higher altitudes. These radial velocities will then form the basis of further spectral analysis, to be discussed herein.

Appendix S1 gives an overview of some technical aspects of the radars used, adopting the Abitibi Canyon radar as an example. Many of the features, such as peak power, measurement mode, duty cycle, height resolution, number of beams and ranges covered, are common to all radars. One point worth noting here is the high level of ground-signal suppression ( $-120$  dB two-way) built into the design of the O-QNet radars (Hocking, 1997). The Harrow radar, for example, is surrounded by several hundred wind turbines, from 5 to 100 km away, but despite this, the strong signal rejection for objects along the ground ensures that the turbines did not contaminate our signal. This resulted in highly reliable wind data with minimal contamination (e.g., see Taylor *et al.*, 2016).

### 3 | METHODS

The main building blocks for this study were spectra of radial velocities, which were examined on log–log plots of power spectral density versus frequency. The power spectral values under examination can be taken to be linear in log–log coordinates for the frequency bands of interest, so straight-line fits are applied. However, rather than look at mean slopes and determine whether they are on the order of  $-1.5$  to  $-2$ , the focus will be on significant variations from such values. Significant flattening of these slopes can be explained by Doppler shifting of IGWs (FVZ87) (Section 4.1), while significant steepening of the slopes can be explained by a 2-D turbulence model (L99, TO03) utilizing Equation (2) (Section 4.2).

While it was noted above that radial velocities are often used to determine total vector winds by combining multiple radial velocities from different beams, in these investigations the radial velocities will be used directly, since by doing so the number of assumptions made in the production of the final product will be minimized.

The technique used involves determination of these radial velocities, then using data-compensated discrete Fourier transform (DCDFT) spectral analysis to properly compensate for missed data and variable sampling rates (Ferraz-Mello, 1981). This technique uses a Gram–Schmidt ortho-normalization process (e.g., Cheney, 2009) to perform the equivalent of a Fourier transform, but allows data points to have non-equal temporal spacings. The focus will be on the use of off-vertical radar beams, following Smith *et al.* (1985; 1987). This is partly because this yields the most useable data, and partly because it gives greater sensitivity in subsequent tests, as will be explained shortly.

Data were chosen primarily from one beam only, nominally “north” in this work (with some minor exceptions). Note that, due to local constraints during construction, the “north” beam may not be true geographic north; nevertheless, the beam’s azimuthal orientation is well known ( $\pm 0.5^\circ$ ) for each radar, and is within  $\pm 45^\circ$  of geographic north. Only one beam is used for any selected radar because, if data from different beams are mixed, there is a risk that, by recording in different spatial regions of the sky, the quality of the data will be degraded. However, because different sampling strategies were employed at different times in order to produce optimum coverage of all heights for weather forecasting applications, the resultant radial velocities are only available in any one mode on any one beam and at any one height approximately every 4–7 min, at slightly irregular data steps, and sometimes at even lower data acquisition rates. Nevertheless, there are compensating circumstances as well. For example, different modes may overlap in height, allowing more data at

some heights. In particular, the data at 4–7 km altitude are obtained using both “low-altitude” and “high-altitude” modes, so that these altitudes are sampled more frequently than altitudes above and below this band.

The net result of using these different modes is that our accepted radial velocities are quasi-randomly distributed in time, with spacings between successive points varying from ~5 min out to as much as 30 min, depending on altitude, availability of scatterers and noise/contaminant effects. At times, the radars missed data due to power failures etc., and this also produced temporal gaps.

Generally, it was found that about 1,200–2,000 reliable points per month per height per beam could be recorded, with a mean number of points over our entire radar set of 1,632 per height and per month. On some occasions, using special recording strategies, counts higher than 2,000 per month were obtained, and on 5% of occasions (during special experiments, such as occasions when the system was run in a three-beam mode instead of a five-beam one), rates as high as 4,000 radial velocities per beam per month per height were achieved. To better comprehend the results, a simple spectral model was developed, which could be used to ascertain accuracies in the analyses. This model is described in Appendix A, and will be discussed in greater detail in Section 5.

## 4 | THEORY OF GRAVITY WAVES AND 2-D TURBULENCE RELEVANT TO OUR ANALYSIS

### 4.1 | Gravity waves: Essential background

The studies presented in this article are based on spectra of radial velocities determined using windprofiler data, which are then compared with model simulations. In regard to modelling, previous studies of Doppler shifting of the intrinsic IGW spectrum will be employed. Such studies have been performed by, for example, Scheffler and Liu (1985; 1986), and FVZ87. The work of FVZ87 has been adopted because their results are presented in ways that are most amenable to comparisons with our observational data. Figure 4 from FVZ87 is re-calculated and re-plotted here (with important adaptations) as Figure 3, and will be used as a reference throughout the work. Note the sharp cut-offs on either side: these graphs show only the gravity waves; evanescent external gravity waves and possibly planetary waves exist to the left of  $\omega/f = 1$  but are not included in the figure. They will be discussed again shortly.

Various authors have proposed forms for gravity wave intrinsic spectra, but all are largely similar, although

presented in different ways. These include gravity wave spectral forms presented by FVZ87, Walterscheid and Hocking (1991) and Gardner *et al.* (1993). The model given by FVZ87 is simpler but quite appropriate for our purposes, as it provides for the easiest comparisons with our data.

FVZ87 specified a spectral energy density as a function of intrinsic frequency and horizontal wavenumber of the form

$$E^h(k, \omega') = E_0(p-1)f^{p-1} \frac{(\omega')^{-p} (t-1)}{k_* \left(1 + \frac{k}{k_*}\right)^t}. \quad (3)$$

In this equation,  $\omega'$  is the intrinsic angular frequency (i.e., as seen by an observer moving with the mean wind),  $f$  is the inertial angular frequency,  $k$  is the wavenumber,  $k_*$  is a fixed value of  $k$  and is referred to as the “characteristic horizontal wavenumber” and  $t$  is another constant. (Although “ $t$ ” can be confused with time in Equation 3, here it is not time; the notation of FVZ87 has been followed).

FVZ87 integrated Equation (3) over all  $k$  to give a function which depends only on  $\omega$ , and we refer to that spectrum as  $E_h(\omega)$ . In this work, the frequency dependence is most important, so the term  $(\omega')^{-p}$  is paramount. The value of  $p$ , which represents the negative of the slope of the intrinsic  $\log_{10}$  spectral density as a function of  $\log_{10}$  frequency, is sometimes taken as 5/3, but is also taken as 2 at other times; FVZ87 recommended a value of 2, since it is mathematically convenient (see just prior to equation [23] in their article); the exact value can be considered as unknown but probably lies between 5/3 and 2. A value of  $t = 3$  is recommended. FVZ87 integrated this function over the  $k$ -spectrum for different mean winds, and in the end produced their equations (30) to (35), which show the frequency dependence of the wavenumber-integrated Doppler-shifted spectrum. These equations will not be reproduced here; rather, Figure 3 in this article will be the main source of reference.

It is important to note that Figure 3 does not make any estimates of expected wave amplitudes that can be used here. The graphs are scaled relative to a quantity  $E_0$  which equals the total kinetic and potential energy per unit mass in the system, but the value of  $E_0$  is left as arbitrary. For the purposes of this article, the *ratios* of the energy densities in Figure 4a,b can be compared in an absolute sense.

Of primary importance is the grey shaded area in Figure 3a,b, which represents the region of best experimental response of the radars, for reasons related to sampling efficiencies, as discussed in Section 2 and Appendix S1. The inset box labelled “S” shows qualitatively the slopes in the region of the graphs outlined by the larger box with dashed borders in Figure 3a. It can be seen that, while the shaded region is our most experimentally sensitive region, it is *also* the most sensitive region *for the model*, as

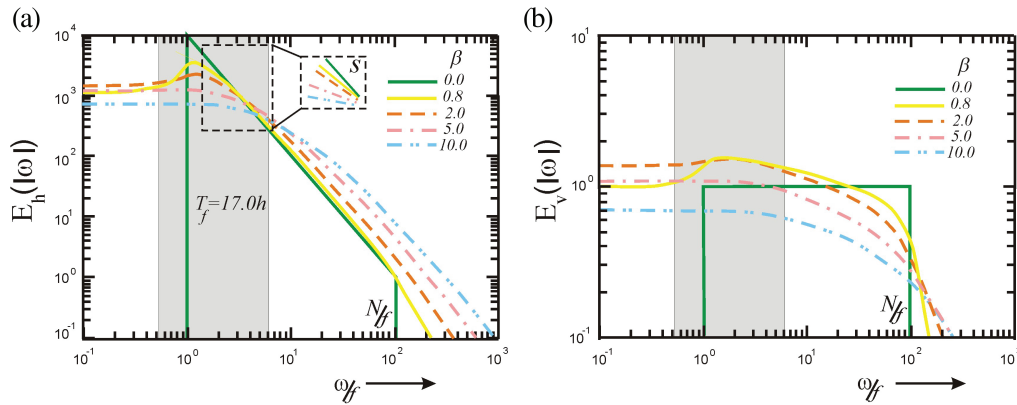


**FIGURE 3** Doppler-shifted IGW spectra as viewed by a stationary observer for various degrees of Doppler shifting, plotted using the formulas of FVZ87: (a) spectra of horizontal velocities, and (b) spectra of vertical velocities. Here,  $\beta$  is the ratio of mean wind speed divided by typical wave phase speed, while  $\omega$  is the wave frequency,  $f$  is the inertial frequency, and  $N$  is the Brunt–Väisälä frequency. All frequency units may be considered as radians per second in this graph, but have been normalized relative to the inertial frequency throughout. The inertial frequency has a corresponding period of 17.0 hr, which is the value at the approximate midpoint of the O-QNet (actually 16.97 hr at 45° N). The units of  $E_h$  and  $E_v$  are  $m^2 s^{-1}$  and are scaled using a quantity denoted as  $E_0$  by FVZ87 (see text for details). The inserted box labelled “S” in (a) shows approximate mean slopes in the region denoted by the larger box with broken borders. The grey shaded region shows the spectral range of our best data

the mean slopes of the model show the greatest variability as a function of  $\beta$  in this region ( $\beta = \bar{u}/c_*$ , where  $c_*$  is the representative phase velocity of waves travelling in some prescribed direction and  $\bar{u}$  is the component of the mean wind in that direction).

The model presented by FVZ87 assumes that the gravity waves passing over the radar are essentially distributed isotropically. Sources are assumed to occur in all directions, and to radiate isotropically (e.g., see Piani *et al.*, 2000, Figures 4, 5 and 8, which show general (though not complete) isotropy). This means that, in any part of the spectrum, waves are Doppler shifted on average equally in the positive and negative directions.

In addition to Figure 3, some extra information needs to be considered. First, it needs to be recognized that the waves obey a dispersion relation. These have various levels of complexity, depending on the assumptions used in solving the Navier–Stokes equations. Here, equation (43) from Walterscheid and Hocking (1991), has been chosen. This is quite general and describes non-hydrostatic compressible flow on an  $f$ -plane with Rayleigh drag. The equation of most importance is

$$\tilde{m} \left( \tilde{m} + \frac{i}{\bar{H}} \right) = \frac{\omega_R}{\omega} \cdot \frac{(\bar{N}^2 - \omega^2)}{(\omega_R^2 - f^2)} k^2 + \frac{\omega^2}{\bar{c}_s^2} \quad (4)$$

where  $\tilde{m} = m - \frac{2i}{\bar{H}}$ ,  $m$  being the vertical wavenumber,  $\bar{H}$  is the scale height of the atmosphere, and of course  $i = \sqrt{-1}$ . The term  $\omega_R$  is equal to  $\omega + i\alpha$ , where  $\alpha$  is the Rayleigh drag coefficient. All angular frequencies in this equation

are intrinsic ones (no Doppler shifting). Finally,  $\bar{c}_s$  is the speed of sound. Equation (4) will be revisited shortly.

Two final points need to be recognized in regard to Figure 3. The first point arises in regard to an assumption usually made with windprofiler radars. In many applications, the vertical wind component is set artificially to zero, and all of the radial velocity measured by the radar is ascribed to the horizontal wind. The approximation gets better for lower frequencies. However, since the effect is frequency dependent, it does lead to modest biases when slope fitting to the spectra. Using the relative energies between  $E_h$  and  $E_v$  shown in Figure 3, it is shown in Appendix S2 (following Van Zandt, 1985) that this will lead to a systematic bias, and our measured slopes will be too shallow relative to the true  $E_h$  slopes by about 3%. This correction will be applied later to compensate for such systematic errors.

Secondly, the FVZ model assumes a sharp cut-off in the intrinsic spectrum at the inertial frequency ( $\omega/f = 1$  in Figure 3). In a realistic wave model, the region  $\omega < f$  will be occupied partly with waves which decay exponentially with distance from their source ( $m$  will be imaginary in Equation (4); see Appendix S2). These are called “external gravity waves”. The region will also contain Doppler-shifted IGWs and possibly even Doppler-shifted planetary waves. The spectral behaviour in this region is unknown; non-linear effects and wave saturation may be important in defining it (e.g., Fritts and Alexander, 2003), and it is possible that some aspects of planetary-wave generation (usually reserved for periods of 2 days and more) may also apply even at  $\omega = f$ . The behaviour in this

frequency region is therefore best left to observation, and this will be revealed in Section 5.2.1.

## 4.2 | Relevant 2-D turbulence theory

We now turn to examine the effect of a mean wind on a 2-D turbulence spectrum which is carried with the mean motion; the possibility of IGWs will be temporarily ignored. The spectral form expected for an atmospheric region drifting over a radar at speed  $\bar{u}$ , in which 2-D turbulence dominates the internal motions, was presented in Equation (2). Figure 4 shows the spectra measured in frequency space (as seen by a radar) for various drift speeds ranging from 1 to 30  $\text{m s}^{-1}$ . Typically, weather systems drift at speeds of  $\sim 5\text{--}20 \text{ m s}^{-1}$ ; for example, knowledge of Canadian weather from the O-QNet assists with 7-day forecasts in Europe (an 8,000 km distance), as Canadian weather systems reach Europe (changed in form but not completely degraded) in about 7–10 days. Other evidence supporting these estimates is presented in figure 7 of Chang *et al.* (2002) and Hoskins and Hodges (2018).

The curves are dominated by a  $-3$  power law to the left and  $-5/3$  power law to the right. The approximate intersection points of the two laws are indicated by grey squares.

The values for  $d_1$  and  $d_2$  assumed in Equations (1) and (2) have been taken from L99, which use MOZAIC data (Marenco *et al.*, 1998), and these values also produce a reasonable fit to Nastrom and Gage (1985). It is prudent

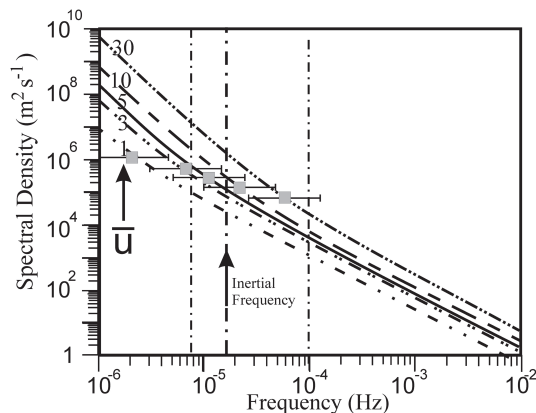


**FIGURE 4** Graphs of  $k$ -spectra due to 2-D turbulence (see Equation (2)) as seen in the frequency domain by a profiler radar, for different drift speeds of the overlying weather system, and using Taylor's frozen-in hypothesis. Values of  $\bar{u}$  are indicated on the left. Grey squares show approximate points of intersection of the  $k^{-3}$  and  $k^{-5/3}$  portions of the spectral field; the error bars are discussed in the text. Vertical dash-dot lines define the approximate spectral range in which our analysis was applied. The inertial frequency (Hz) is also shown

for us to test whether our results are sensitive to the values of these parameters. We will examine the impact of variations in the ratio  $d_1/d_2$  of a factor of 10 (i.e., varying from  $[\sqrt{10}]^{-1}$  to  $\sqrt{10}$  times the currently assumed value). Such a range gives allowance for different data sets to have different values of  $d_1$  and  $d_2$ , although as discussed by TO03, there is a general belief that there is some degree of universality about the values. Allowing for variations of a factor of 10 allows us to consider a reasonable level of natural variability but still maintains some possibility of universality.

In log-log space, the limiting cases of Equation (1) at very low and very high wavenumbers comprise two straight lines (asymptotic limits) of the type  $\log_{10}[E_L(k)] = a_L x + b_L$  and  $\log_{10}[E_H(k)] = a_H x + b_H$ , where  $x = \log_{10}(k)$ , with “L” referring to the lowest wavenumbers and “H” referring to the highest wavenumbers. Hence,  $a_L = -5/3$  and  $b_L = \log_{10}(d_1)$ , while  $a_H = -3$  and  $b_H = \log_{10}(d_2)$ . These two lines intersect at a value  $x_{\text{int}} = (b_L - b_H)/(a_H - a_L)$ , so in our case the value of  $k$  at the intersection satisfies  $\log_{10}(k_{\text{int}}) = -3/4 \log_{10}(d_1/d_2)$ . Converting to the frequency domain to prepare us better for the experimental result later, we denote the frequency in Hz as  $\nu$ , then assume that the scales drift over the radar with speed  $\bar{u}$ . Then the measured frequency is  $\nu = \omega/(2\pi) = \bar{u}k/(2\pi)$ , so the point of intersection of the two asymptotic curves occurs where  $\log_{10}(\nu_{\text{int}}) = -3/4 \log_{10}(d_1/d_2) - \log_{10}(2\pi/\bar{u})$ . These points have been plotted in Figure 4 for the given values of  $d_1$  and  $d_2$ , but in addition cases where  $d_1/d_2$  is multiplied by  $1/\sqrt{10}$  and  $\sqrt{10}$  times, as discussed in the previous paragraph, have been discussed. These two cases represent the extremities of the “error bars” shown in Figure 4.

The actual graphs shown in Figure 4 show only the cases for  $d_1$  and  $d_2$  as prescribed following Equation (1); the graphs for  $d_1/d_2$  when multiplied by  $1/\sqrt{10}$  or  $\sqrt{10}$  have not been added, in order to reduce clutter. They look similar to the ones shown, but transition from the  $-5/3$  power law to the  $-3$  power law at different points; for example, when  $d_1/d_2$  is smaller, the  $k^{-3}$  portion becomes significant at higher frequencies, so the transition point occurs more to the right in the figure. For the modified cases of  $d_1/d_2$ , the correct frequency values of the transition points are shown as the end-points of the error bars: since it is only the transition frequencies that are most important, the correct vertical positioning is not given, again to avoid clutter.

The vertical dash-dot lines show upper and lower limits to the region of the graphs that will be analysed later. The slope changes in this region, but only modestly, so in order to be able to compare this model with our results, slopes of best-fit straight lines across this spectral band for different values of  $\bar{u}$  have been determined.



For speeds of 1, 3, 5, 10 and 30 m s<sup>-1</sup>, the slopes were  $-1.82 \pm 0.01$ ,  $-2.09 \pm 0.02$ ,  $-2.30 \pm 0.02$ ,  $-2.55 \pm 0.02$  and  $-2.83 \pm 0.01$ , respectively, for the cases where we used  $d_1$  and  $d_2$  as described after Equation (1). Multiplying the ratio ( $d_1/d_2$ ) by  $\sqrt{(10)}$  or  $1/\sqrt{(10)}$ , as discussed above, did not change the range of values of the slopes; they were still in the approximate range from  $-1.7$  to  $-2.8$ , and (not surprisingly) never became greater than  $-1.67$  or less than  $-3.0$ .

It could be argued that these drift speeds are too small to allow the application of Taylor's frozen turbulence hypothesis. This assertion will be checked using a scheme proposed by Lin (1953) and Lumley (1965). In Lumley (1965), it is proposed that, for a turbulent wavenumber  $k_{\dagger}$ , the wavenumber can be considered to be amenable to application of Taylor's "frozen turbulence" hypothesis if the integrated kinetic energy in the spectrum between  $\frac{1}{2}k_{\dagger}$  and  $\frac{3}{2}k_{\dagger}$  (which will be referred to as  $[u'_{\dagger}]^2$ ) is substantially less than  $\bar{u}^2$  (Lumley's equation (4)). The anti-derivative of Equation (1) is

$$I_E(k) = -\frac{3}{2}d_1k^{-2/3} - \frac{1}{2}d_2k^{-2} + c,$$

( $c$  being an arbitrary constant), which will now be employed. A representative value of the frequency close to the left-hand vertical dash-dot line of Figure 4 was chosen; in this case, we chose  $\nu_{\dagger} = 1.5 \times 10^{-5}$  Hz. Then, for a chosen value of  $\bar{u}$ , the associated wavenumber  $k_{\dagger} = \nu_{\dagger} \times 2\pi/\bar{u}$  was found. Lumley (1965) recommended determining  $k_{\dagger} \times E_1(k_{\dagger})$  as the "kinetic energy" associated with the band around  $k_{\dagger}$ , but here the energy was found by integrating between  $\frac{1}{2}k_{\dagger}$  and  $\frac{3}{2}k_{\dagger}$ , which gives better accuracy. Of course this is just the kinetic energy per unit mass in the parallel spectrum, rather than the total energy density due to all three components of the velocity vector, but here Lumley (1965) is followed; we only seek a suitable test parameter.

Evaluating  $I_E(k)$  at  $k_1 = \frac{1}{2}k_{\dagger}$  and  $k_2 = \frac{3}{2}k_{\dagger}$  and taking the difference (using values of  $d_1$  and  $d_2$  from Equation (1)) gives the integrated energy  $[u'_{\dagger}]^2$  over the band between  $k_1$  and  $k_2$ .

The quantity  $[u'_{\dagger}]^2/\bar{u}^2$  was then found. For values of  $\bar{u}$  between 30 and 5 m s<sup>-1</sup>, the ratio varied only modestly from 0.06 to 0.12. For  $\bar{u} < 5$  m s<sup>-1</sup>, the ratio became noticeably larger, being 0.18 for  $\bar{u} = 3$  m s<sup>-1</sup> and 0.67 for  $\bar{u} = 1$  m s<sup>-1</sup>. If  $\nu_{\dagger}$  was taken to be in the region around the transition from a  $-5/3$  to  $-3$  power law, where  $k_{\dagger}$  was greater, the ratios were typically 0.05 and less.

Lumley (1965) did not give numerical values for acceptable ratios, but Wyngaard and Clifford (1977) did. Using boundary-layer anemometer data, these authors examined cases with  $[u'_{\dagger}]^2/\bar{u}^2 \approx 0.01$  to 0.1 (their table 1 and

underlying text). They then determined the degree to which spectra were distorted for the various cases in their table 2. Distortions of the longitudinal spectra were determined to be on the order of 1% to 11%, with largest distortions occurring for largest values of  $[u'_{\dagger}]^2/\bar{u}^2$ . It is unclear whether these distortions affected the magnitudes, or slopes, or both. However, even if the slopes were affected by 10% (worst-case scenario), this will alter slopes around  $-3$  by at most 0.3 (i.e., between  $-2.7$  and  $-3.3$ ), and generally by less. In regard to the  $-5/3$  law, the distortions would be less than 5%. For our level of interest, this is sufficiently small for us to develop guidelines that will help distinguish 2-D turbulence from IGWs.

As a point of interest, the analysis was extended to lower values of  $\nu_{\dagger}$  (down to values of  $5 \times 10^{-6}$  Hz and lower, corresponding to periods longer than 2 days). In these cases, the ratio  $[u'_{\dagger}]^2/\bar{u}^2$  became rapidly larger, often being 50–100% and climbing as  $\nu_{\dagger}$  decreased. This suggests that, for lower frequencies outside our band of interest, the Taylor hypothesis may collapse, a result that experimental data will later partly corroborate.

It is therefore concluded that, for weather system drift speeds of  $\sim 5$ – $20$  m s<sup>-1</sup>, and for a system purely comprising 2-D (and/or possibly 3-D) turbulence, and for spectra analysed in the band indicated in Figure 4, slopes of approximately  $-1.8$  to  $-2.7$  are to be expected. The primary cause of these steep slopes is the  $k^{-3}$  part of the 2-D turbulence  $k$ -spectrum; without it, slopes steeper than  $-2$  cannot be obtained. To account for fitting errors, we will set the limit at  $-2.1$ . Then, slopes less than  $-2.1$  are proposed to represent 2-D turbulence, either in the  $k^{-3}$  part of the spectrum or in both the  $k^{-5/3}$  and  $k^{-3}$  portions.

### 4.3 | Mixed spectra

In Sections 4.1 and 4.2, the frequency spectra expected due to IGWs (4.1) and 2-D turbulence (4.2) were considered separately. Limits were set on allowed ranges of slopes; purely IGWs lead to shallow spectra in our region of interest, while purely 2-D turbulence leads to steeper slopes (negative in all cases). Here, we wish to make some comments in regard to the possibility of a mixture of the two mechanisms.

First, it is important to note also that, when purely  $k$ -spectra are examined, *both* the 2-D turbulence model and the IGW model include a  $k^{-3}$  component (see Equations (1) and (3)), but they manifest in very different ways: in the 2-D case they map according to the Taylor frozen turbulence hypothesis over a wide range of frequencies, producing some  $\omega^{-3}$  spectral portion, while in the IGW case the  $k^{-3}$  component is masked by the effects of the IGW dispersion relations and the measured IGW frequency spectrum shows no  $\omega^{-3}$  component.

The 2-D spectrum should always be present, but will often be overpowered by the IGW spectrum when IGWs are present: as the spectral amplitude of the IGW portion increases, the intercept with the  $\omega^{-3}$  portion moves to the left in Figure 4, and the spectral interval between this intercept and the “Taylor frozen turbulence breakdown point” (discussed in the last section, i.e.,  $\nu_{\dagger} \sim 5 \times 10^{-6}$  Hz) narrows. Consequently, a distinctive 2-D turbulence  $\omega^{-3}$  portion is often not visible, although it does exist to sufficient degree that it impacts the fitting of linear slopes to the spectra.

If, in addition, a realistic case comprising a mixture of 2-D eddies and IGWs (possibly with Doppler shifting incorporated) is considered, the radar spectra may get complicated: if, for example, the nominal  $\omega^{-5/3}$  portion of the spectrum were dominated by IGW and the  $\omega^{-3}$  portion by Q-G turbulence, a measured power law of around  $\omega^{-5/3}$  could send mixed messages about the relative contributions of the two phenomena; a flattened slope due to the IGW, coupled with a  $\omega^{-3}$  Q-G turbulence contribution, could even average out around  $-5/3$ , for example. Furthermore, in the absence of Doppler shifting, a  $\omega^{-5/3}$  or  $\omega^{-2}$  spectrum due to IGWs may be hard to separate from a 2-D turbulence model with a  $\omega^{-5/3}$  power law. So clearly there will be cases where a distinction between the causes of the oscillations may not be possible, but we have found some criteria which will enable significant distinction between the models in a valuable range of situations.

Specifically, it can safely be proposed that (a) slopes less than  $-2.1$  in the log-log spectral frequency space are strongly suggestive of 2-D turbulence (including Q-G

turbulence), (b) slopes greater than  $-1.5$  are strongly suggestive of Doppler-shifted IGWs and (c) intermediate values will need additional investigation to resolve their cause. If results show both categories (a) and (b) at different sites and/or times, then it will be apparent that the atmosphere comprises both 2-D turbulence and IGWs, though not necessarily at the same time. It will be seen in the following analyses, with the use of 11 different stations, that there is more than adequate room for a wide range of revealing scenarios. At times, some pattern recognition can be used to help resolve the models (see later).

## 5 | ANALYSIS DETAILS

The details of the experimental technique will now be presented.

### 5.1 | Analysis: Basic procedure

Data were divided into monthly segments, and DCDFDT analysis of these monthly time series of radial velocities was implemented for the nominal “north” beam, for all sites and all altitudes.

Examples of DCDFDTs of our radial velocities produced using Ferraz-Mello decomposition are shown in Figure 5 (black solid lines). The spectra were taken at (a) Negro Creek in June 2010, at 8 km altitude, and (b) Eureka in February 2017 at 2 km. These spectra were not chosen because they are particularly good or bad, but were simply

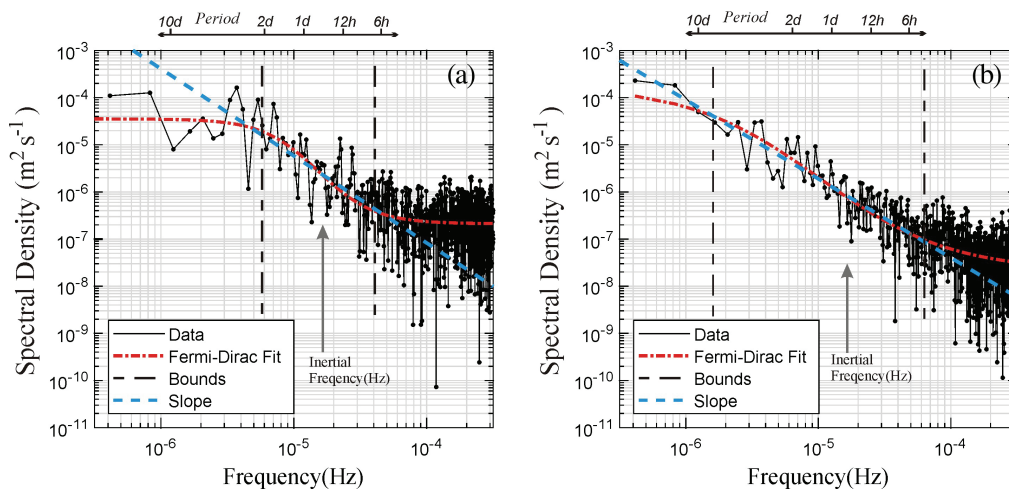


**FIGURE 5** DCDFDTs overlain with fitting procedures. Each graph represents real data. (a) A sample spectrum using some real data for the case in which the power spectral densities (PSD) become flat at small frequencies ( $< 5 \times 10^{-6}$  Hz), and where the PSD enter the noise at a frequency of  $\sim 4 \times 10^{-5}$  Hz. (b) Another real data set, this time with the PSD maximizing on the left and then generally decreasing as the frequency increases to the right; the PSD enters the noise in this case at a frequency of around  $6 \times 10^{-5}$  Hz. In each case the DCDFDT is given by the black solid line. The so-called Fermi-Dirac fits are shown as dash-dot lines. The cut-offs (bounds) used for straight-line fits are shown by vertical broken lines, and the actual straight line fit is shown by the sloping dashed line

selected randomly. The apparent “straight-line” sections are statistically significant, with values of the Pearson regression coefficient of 0.42 and 0.64, respectively; more details about the statistical significance will be discussed in Section 5.2.2.

Each spectrum is different, so care is needed in isolating and fitting the relevant straight line. In creating the power spectra, a Hamming window was generally used for all transforms, although a Hann window (Bendat and Piersol, 2000; Wright, 2014) was also tested. Of particular note is the region between the two vertical broken lines in each graph, where an approximate straight-line behaviour is seen, as illustrated by the sloping dashed lines. These regions correspond approximately to the grey regions shown in Figure 3, but intrude somewhat more to the left of the inertial frequency. Visually, one can notice a break in the behaviour at a frequency of order  $10^{-4.4}$  Hz (a period of 7 hrs) in 5(a), and a frequency of  $10^{-4.2}$  Hz (period of about 4 hrs) in 5(b). Note that frequencies are given in Hertz here and in subsequent discussions, as these were the outputs of the analysis (used for reasons of computational efficiency); previous theoretical discussions used radians per second. Break-points on the right often occurred at frequencies up to  $\sim 10^{-4}$  Hz, corresponding to a period of 2.8 hrs.

To the right of the right-hand break-points, the spectra are highly fluctuating, on average flat and dominated by noise. This is not just a limitation associated with the radial velocities, but also a noise limitation associated with the Ferraz–Mello algorithm and the irregularity of the data points. This will be discussed in connection with Appendix A, but at this stage, it is noted that the radar itself is capable of measuring to much higher frequencies if a different data acquisition cycle is used. For example, if only one beam were used continuously, a data rate of one point per minute would be achieved and the analysis could easily resolve periods as short as 5 min. However, because the radar was set up for multiple different applications including weather prediction, a more complex set of acquisition cycles which was not optimum for this particular experiment was necessary. Nevertheless, as will be shown, the data are adequate in their current form for analysis purposes.

Our procedure comprised two main steps: first, it was necessary to identify the frequency band of interest, and the second step was to apply a standard least-squares straight-line fit to the data within that frequency band. As seen by looking at Figure 5a,b, there are essentially two break-points: one on the right, where the signal meets the noise (discussed above), and another on the left, where the spectrum tends to flatten out at frequencies below the inertial frequency. The flattening always happens to the left of the inertial frequency, though the break-point can

in some cases be a factor of 3 or 4 times below the inertial frequency. (The reason for this flattening on the left could be in part related to the breakdown of the Taylor “frozen-turbulence” hypothesis, which was seen to occur at frequencies below  $\sim 5 \times 10^{-6}$  Hz; see the discussion following Figure 4, towards the end of Section 4.2. Regardless, it does not affect our analysis of the spectral band of interest.)

The procedure for determining these break-points in a non-subjective manner will now be discussed.

## 5.2 | Fermi–Dirac fits and slope determination

### 5.2.1 | Identification of the spectral band

In earlier studies, the two break-points were determined visually (Wright, 2014). This makes the task subjective, which is undesirable, but was nevertheless of value. By viewing many hundreds of such spectra (Wright, 2014), it was possible to determine the behaviour in the region immediately to the left of the inertial frequency (loosely referred to as the “external wave region”, though this is used as a descriptor and does not infer that this region is dominated by such waves). In Section 4.1, it was recognized that Figure 3 does not consider this region at all, but it was noted that it is likely to be inhabited by evanescent waves as well as Doppler down-shifted IGW and up-shifted planetary waves. A key finding from these visual studies was that the approximately constant slopes close to and above the inertial frequency  $f_1$  (the inertial frequency in Hz, while  $f$  is used for units of rad/s) continue on into the frequencies below the inertial frequency, typically down to  $f_1/2$  or even  $f_1/3$ : Figure 5a shows a case where the straight-line behaviour is evident down to  $f_1/3$ , then the curve flattens at smaller frequencies. In Figure 5b, the mean slope persists even down to  $f_1/10$ , although this is exceptional and may be due to the low altitude of 2 km. Indeed Figure 5b does not even appear to flatten at all; however, by repeating the DCDFt using an even longer data set, well in excess of 1 month (and even up to 1 year), it was possible to demonstrate that even this extreme example did indeed flatten at  $f < 5 \times 10^{-7}$  Hz: the flattening was ubiquitous to some degree throughout our data set. As noted, it is possible that this flattening may be partly a result of the breakdown of Taylor’s “frozen turbulence” hypothesis, as discussed towards the end of Section 4.2 (possibly coupled with the natural Eulerian decorrelation [rather than Lagrangian decorrelation] of weather systems over periods of 2 and more days).

The reasons for this extension of the linear slope to the left of  $f_1$  are unclear and might involve saturation, non-linear processes and other complications. We have no obligation to explain this behaviour here: we simply need to confirm that the linearity exists. Such a continuous behaviour is of course expected for 2-D turbulence (Figure 4), but in that case these slopes will still need to be steep, with values less than  $-1.8$  (see Section 4.2). It must be noted that this frequency region is the most reliable of the radar data; experimental error is not a cause of these effects. For our purposes, the extended linear region does allow extension of our zone of study, and in defining our analysis band, frequencies as low as  $f_1/3$  will be allowed (after verification). Further evidence of the suitability of these limits will be provided retrospectively later in Section 6.4.

Following these earlier visual studies, a second and more robust method was developed for determining the break-points. A function was developed of the type shown by the dash-dot lines, labelled “Fermi–Dirac fit” (F–D fit) in Figure 5a,b. This function is essentially a hyperbolic tangent profile with an offset, but will be referred to as a Fermi–Dirac function following its use in specifying electron density occupancy in quantum mechanics (and it will also be used here in the context of an “occupancy” diagnostic). It has the form

$$F_D(f_r) = \frac{a}{1 + \exp\left(\frac{f_r - f_c}{c}\right)} + d \quad (5)$$

where  $f_r$  is the frequency in Hz,  $f_c$  is a central frequency of the curve,  $a$  is an “amplitude term”,  $c$  is a measure of the width of the step and  $d$  is an offset:  $f_c$ ,  $a$ ,  $c$  and  $d$  are all fitting parameters and are varied to optimize the fit. Such a fit was applied to our spectra, then the break-points were found as follows: The F–D fits are vertically limited on the left and right, and the limiting ordinate values will be denoted as  $P_L$  (on the left) and  $P_R$  (on the right). The quantity  $\zeta = 0.1 \times (P_L - P_R)$  is then found, and subsequently the frequencies at which the fitted curve attains values of  $P_L - \zeta$  and  $P_R + \zeta$  are determined. These are the points marked in the figures by the vertical broken lines.

It would have been possible at this time to use the slope of the Fermi–Dirac fit at the midpoint as a measure of the slope, but it was found to be more practical to isolate the spectrum between the two vertical broken lines and then fit a straight line afterwards, since with this approach the impact of frequencies outside of the chosen region is minimized. It is this slope which was used for subsequent analysis. These slopes were stored as a function of time and height for all radars. It is important to note that, after the F–D process was used to identify the region to be fitted, the F–D function played no further role in our analysis.

## 5.2.2 | Slope fitting and associated statistics

Since our frequencies were known without appreciable error, slope fitting was achieved using standard Pearson regression. Typical regression coefficients were on the order of 0.3–0.5, and the overall average was 0.39. Fitting errors  $\sigma_a$  were produced for each Pearson-fitted slope “ $a$ ”, and the average error across all the slopes was 0.23, with a standard deviation of 0.12. This will be even further verified in the next sub-section, where modelling studies which revealed a mean error of 0.25 are discussed. The interested reader is referred to Appendix S3 for further details.

The  $p$ -value, which is the probability that the data are really noise, was also determined. Across all of the radars, and out of 13,952 slopes, only 9 cases showed a  $p$  value greater than 0.05, so 99.94% of all slopes were statistically significant at the 95% acceptance level. At even higher significance levels, 97.3% of all slopes were statistically significant at the 99.9% level ( $p < 0.001$ ), which represents a very high level of significance.

All calculations were carried out using Python software. Using Figure 5 as an example, Figure 5a had a slope of  $-1.84 \pm 0.3$ , a regression coefficient of  $R^2 = 0.42$  and a  $p$ -value of  $1.07 \times 10^{-9}$ , so is highly significant, while Figure 5b had a slope of  $-1.63 \pm 0.09$ ,  $R^2 = 0.64$  and  $p = 3.9 \times 10^{-40}$ . Modest alterations of these slopes will be necessary following Section 5.2.3, but the significance levels will not change appreciably.

More specific details about the statistical accuracy of our fits are given in Appendix S3, which includes probability density functions of  $R^2$  and  $p$  across all samples. In addition, Figure S3.5 shows comparisons between fixing the low-frequency cut-off at half of the inertial frequency  $f_1$ , as distinct from using our standard low-frequency cut-off deduced from the F–D procedure (which usually produced a frequency less than  $f_1/2$ ). This agreement demonstrates even further that the results are robust.

## 5.2.3 | Modelling tests of statistical accuracy

To make best use of these data, it was necessary to be aware of any distortions and errors which might arise from the technique. To this end, a computer model simulating the horizontal velocities was developed, then the combined DCDFT/Fermi fitting procedure described above was applied to the model data. This model is discussed in Appendix A and Appendix S4. It provides the ability to determine systematic and random errors associated with the procedures employed (regardless of whether the spectra were due to waves or 2-D turbulence).



An ensemble of 38 representative gravity waves was generated, and the waves were added with random phase combinations. DCDFT spectra were generated from the resultant time series with the intent of producing spectra similar in form to those shown in Figure 5 (also see Figure A1). Having produced such spectra, experimental data sets could be modelled. This included the ability to have randomly sampled data, just as with real data, and to simulate extended periods of missing data. It was also possible to experiment with different percentages (“occupancies”) of data acquisition.

Occupancy rates were defined in terms of the number of time steps with which an experimental data set was recorded, divided by the number of useful points that could potentially have been recorded under optimal circumstances. However, the latter term was not calculated based on the fastest radar acquisition rates; rather, the optimum number of points was set to the number that would be needed to properly simulate all the features that the spectrum might produce, including waves with periods equal to the Brunt–Väisälä period (10 min in the troposphere).

Taking the nominal highest frequency as a gravity wave of period 10 min (at least before Doppler shifting), 5 min can be considered as an optimal sampling (to avoid most aliasing effects). Therefore, 5 min sampling was considered as being a “100% data rate”, and other data rates were represented as a fraction of this rate. This will be referred to as the “occupancy”. Data acquired every 5 min over the period of a 30-day month would result in 8,640 points. Due to the sampling issues discussed in Sections 2 and 3 and the need to provide data for weather forecasting, an average of about 1,632 points per month per height per beam was found, or a 19% occupancy. At some heights where different acquisition strategies overlapped, it could be more than this, and during three-beam applications this could rise to 25% and more, but in general the occupancy can be considered to be around 20%. Extensive tests have verified that all radar acquisition modes (mono-pulse, short pulse, long-pulse, pulse-coded, etc.) produce equally reliable radial velocities, and it is suitable to mix such data. An example of such mixed data is shown in figure 12.8 of Hocking *et al.* (2016), where it may be seen that the data blend cleanly into each other.

The model presented in Appendix A was applied using different occupancy rates from 100% down to 5% (additional specific details are given in Appendix S4). Occupancy of 100% corresponded to points regularly spaced at 5 min intervals, and showed the same results with the DCDFT as could be achieved with a standard FFT. Lesser percentages corresponded to cases with more data gaps, where the gaps were randomly chosen or even selected as windows of missing data.

In this paragraph, the focus will be on cases with ~20% occupancy. Two main effects were apparent in the modelling studies. The first was that the slope deduced from the model was slightly flattened relative to the true slope, and the second was that the noise level increased as the occupancy was reduced. Appendices A and Appendix S4 discuss these effects in greater detail. The change in slope is expected due to some degree of frequency aliasing, but is not too severe, since the spectrum gets weaker towards the higher frequencies, reducing the impact of high-frequency aliasing; any aliased frequencies are generally moved into regions of higher power and have only modest effect on the overall spectrum. The alteration in slope for the “20% occupancy” case was a decrease (flattening) of ~12% relative to the true value. Recall from Section 4.1 that using radial velocities as distinct from true horizontal velocities produced a further 3% flattening, so the correction from the modelling combined with the correction due to the use of radial velocities is about  $1.12 \times 1.03$ , or close to 1.15. In calculations presented in the following pages, all measured slopes will be rescaled by 1.15, so as to compensate for these effects, with an estimated error of 0.05. A measured slope of  $-1.7$ , for example, corresponds to a geophysical slope (i.e., a true slope of the  $E_h$  curve in Figure 4a) of  $-1.95 \pm 0.08$ . So the expression

$$s_{\text{corr}} = (1.15 \pm 0.05) s_{\text{meas}}, \quad (6)$$

will be used, where  $s_{\text{corr}}$  is the corrected slope and  $s_{\text{meas}}$  is the measured slope determined from the fits to the spectra of radial velocities.

The model also showed a significant increase in noise as the occupancy decreased. This is not surprising, but the model allowed quantification of this effect, and showed a 20 dB increase in noise in moving from 90% to 20% occupancy. While significant, this does not inhibit subsequent analysis, provided that the fitting procedures described above are employed.

In the end, it was concluded that data with occupancy as low as 15% produced reliable slopes once rescaled as above, and in some cases, where the spectral noise was low and the break-points in Figure 5 were at frequencies up to  $\log_{10}$  values of  $-4$ , reliable slope estimates could be achieved down to 12% occupancy. In some cases, data might be good for a period shorter than 1 month, such as in cases where data were continuous for perhaps 25 days but missing for the last 5 or 6 days due to some system failure that required a visit to the radar to restart it. In such cases, occupancy was calculated based on the number of available days of data. To be conservative, real-life cases with less than 15% occupancy will be ignored for detailed analyses, but may at times be displayed for visual purposes.

Finally, Appendix A (and Appendix S4) consider the random errors associated with the technique, and it can be seen there that individual random errors in slope are typically  $\pm 0.25$  (Figure S4.1); this value is consistent with the value of  $\pm 0.23$  discussed in Section 5.2.2, which was derived by a quite different process.

In up-coming contour graphs, a three point by three point running mean (averaging over three height bins and three successive time steps, then sliding on to the next bin and repeating, etc.) is used, which will further reduce errors. By using the central limit theorem, and assuming that adjacent bins can be considered as quasi-independent, the subsequent error for the mean is  $\sim 0.25/\sqrt{9}$ , or about 0.08. Hence the errors in subsequent slopes will be considered to be about  $\pm 0.10$ , with 0.08 coming from this random effect and  $< 0.05$  coming from errors in the slope correction equation; that is, a reasonable estimate of the error is then  $(0.08^2 + 0.05^2)^{1/2} \approx 0.10$  at the one-sigma error level, which may well be an overestimate. The two-sigma error would therefore be 0.20, with a one-sided probability of a random occurrence in excess of the “mean plus  $2\sigma$ ” of 2.3% (as can be obtained from any normal distribution table).

## 6 | RESULTS

### 6.1 | Some interesting structures

To begin, some specific cases of annual and long-term behaviour will be presented. Figure 6 shows examples of density plots (contours) of the slopes produced by the previously described fitting procedures as a function of height and time. As discussed above, nine-point running means (three time steps and three heights) have been applied to the original month-by-month data. Examples of the procedure as applied to the Wilberforce, Harrow and Walsingham radar data for the years of 2010–2013 are shown in Figure 6. As discussed in Section 4.3, slopes greater than  $-1.5$  indicate dominance of gravity waves, whereas slopes less than about  $-2.1$  are suggestive of 2-D turbulence. So in Figure 6, red colours suggest gravity wave dominance. Yellow colours suggest either gravity waves with no Doppler shift, or a mixture of 2-D turbulence and Doppler-shifted gravity waves in roughly equal proportion. The likelihood that there are no Doppler-shifted waves is small, so the second explanation is more likely.

As can be seen, there are many red-coloured cases (corresponding to flat slopes, and high  $\beta$  values in Figure 3), especially for Harrow and Walsingham, particularly above 4–5 km altitude. About 38% of the Harrow graph, and 42% of the Walsingham graph, shows slopes in excess of  $-1.5$ ,

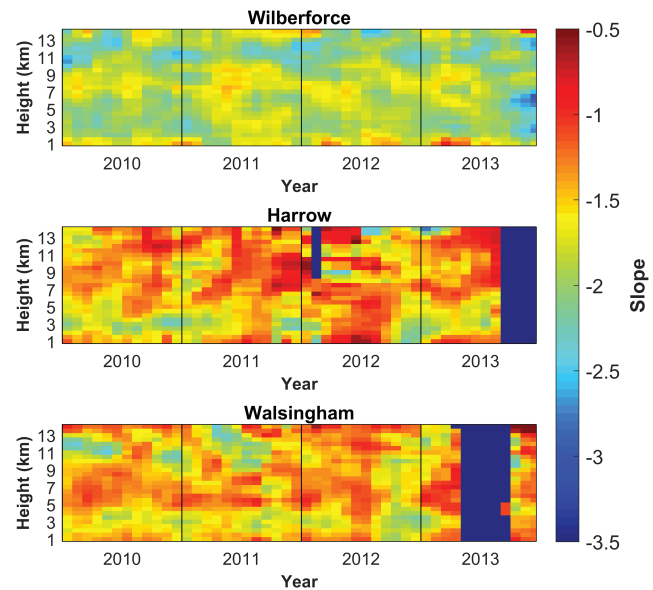
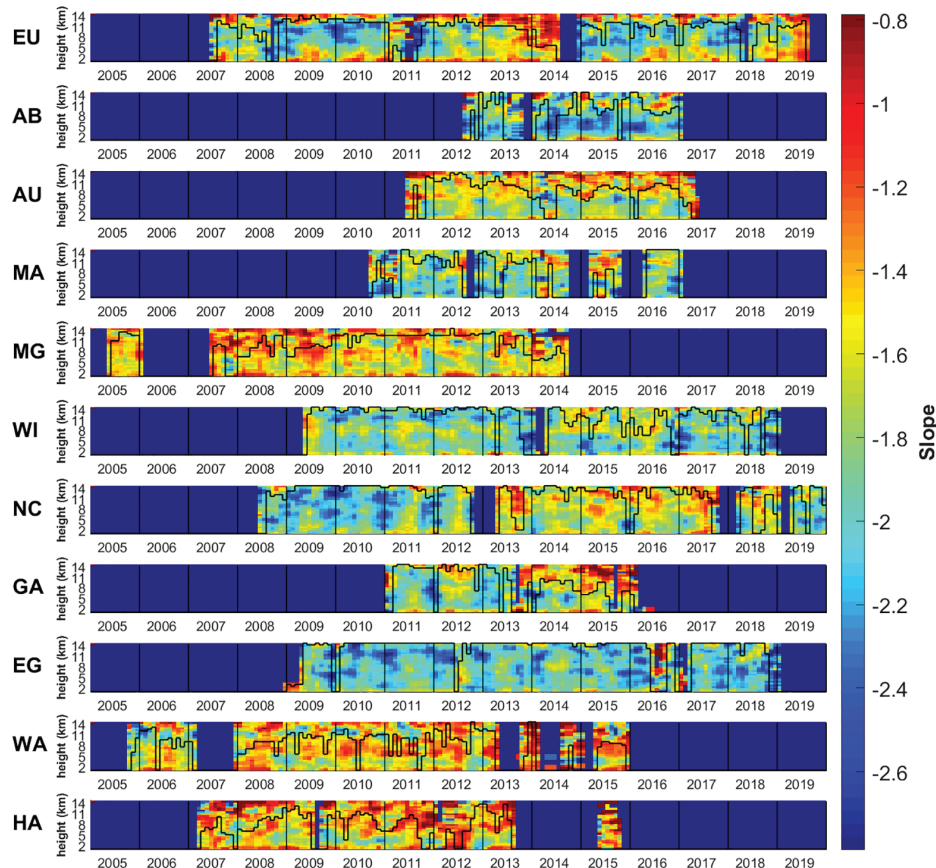


**FIGURE 6** Slopes deduced for the Wilberforce, Harrow and Walsingham radars for the period 2010–2013. Dark-blue areas correspond to missing data

while for Wilberforce the percentage was only 1%. The graphs also show quite repeatable systematic behaviour in the red and yellow colouring for all radars. Despite the fact that the mean slope at Wilberforce is lower, being close to  $-1.7$ , the pattern of reds and yellows is not random but shows some clear structure between 5 and 11 km altitude. Yellow and light-reddish colouring (flatter slopes relative to the surrounding green colouring) appears in midsummer centred at 9 km altitude in 2011, then shows a gradual decrease in height through the following seasons until the beginning of the summer of 2012, when the centroid height reaches 7 km. After this, there is a jump back to 9 km altitude in mid-summer, and the process repeats into 2013. Some evidence of slightly flattened slopes centred at 7–9 km in 2010 is also evident. These results are consistent with a background of 2-D turbulence (green and lighter-yellow colours) with additional gravity wave production (with associated Doppler shifting) being embedded in the yellow–red regions. Such patterns in behaviour are most likely due to IGWs, so patterned structures like this can be an extra discriminator of waves from turbulence, in addition to the criteria discussed at the end of Section 4.2.

The two other graphs (Harrow and Walsingham) show substantial red colouring, indicating substantially flattened slopes. These are both sites close to the shores of Lake Erie, where lake breezes can be quite strong. These could indicate lake-breeze-induced IGWs propagating up into a larger-scale synoptic-scale wind pattern above, resulting in substantial Doppler shifting.

**FIGURE 7** Contour plots of slopes for all sites included in the study, from 2005 to 2019. Sites are ranked according to latitude, highest at the top. From the top, these are Eureka (EU), Abitibi (AB), Aumond (AU), Markstay (MA), McGill (MG), Wilberforce (WI), Negro Creek (NC), Gananoque (GA), Egbert (EG), Walsingham (WA) and Harrow (HA). The black step-like lines across the graphs are discussed in the text. Dark-blue colouring represents missing data



Further discussion in regard to these graphs will be given shortly. For now, however, comparisons between all sites and across all years recorded will be considered.

## 6.2 | Annual observations and site-by-site analysis

Figure 7 shows plots like those in Figure 6, but covering all available data for all radars. Note that Figure 7 uses a different colour palette than Figure 6. The black stepped lines need some discussion. These show demarcations between areas where we have great confidence in our slopes (below the black line) and regions where our confidence is more moderate, but not negligible (above the line). In the former case, even modest structural patterns can be taken to be real, whereas in the latter case small details might be questioned, but bulk features (such as the persistence of shallow slopes around and above the tropopause for several radars) are believable. Also see the discussions following Equation (6) for more details.

Examination of Figure 7 reveals several key items. Each site shows some patterns in behaviour, rather than a random distribution. Flatter slopes (yellows and reds) tend to occur in summer, and some enhancement occurs at some sites at altitudes of 7–11 km (i.e., around and below the

typical tropopause height). Of particular note are flattening of slopes at Walsingham, Harrow and McGill at the upper-tropospheric height, and indeed all radars except Abitibi, Markstay, Wilberforce and Egbert show significant reddening at 12–14 km.

Both Walsingham and Harrow are less than 10 km from the northern shore of Lake Erie. This region is particularly active in regard to lake breezes, which occur here on over 80% of all days in summer (e.g., Sills *et al.*, 2011; Alexander *et al.*, 2018). Over 500 wind turbines which benefit from the breeze have been built in the area for wind power generation. These same lake breezes have been associated with storms and tornado activity, and can even initiate storms (Alexander *et al.*, 2018; Sills *et al.*, 2011; King *et al.*, 2003; Hastie *et al.*, 1999; King *et al.*, 1999). The breezes also have a breeze front, and convergence at lake breeze fronts can trigger vertical motion, release of latent heat and storm development, which can in turn initiate gravity wave activity at the 2 km level and above. The overall flow pattern is helical as a function of height, involving significant shear (Sills *et al.*, 2011). Furthermore, summertime lake breeze flow near the surface is generally from the south-west, while at ~850 hPa (~1.2–1.5 km altitude), where the overlying synoptic flow occurs, winds are more often from the NW (Sills *et al.*, 2011, Figure 5) adding more shear at the top of the breeze.

Importantly for our work here, these variations in flow directions with height will lead to substantial Doppler shifting of any IGW that pass through them, which accounts for the slope flattening discussed above for Walsingham and Harrow. Other studies have also recognized lake and sea breezes as generators of Kelvin–Helmholtz billows, IGW and also acoustic waves (Burrows *et al.*, 2002; Miller *et al.*, 2003).

It is important to note here that Harrow has its “north” beam aligned at 41° west of north, while the “north” beam at Walsingham is aligned at 14° west of north, so the somewhat common behaviour at each site is not due to beam alignment; the main common feature is their proximity to the lake shore.

Mariani *et al.* (2018) observed that lake breezes at Lake Ontario seem a little shallower in height, rising to only ~300 m. The only site that was close to Lake Ontario was north of Gananoque, and that is north-east of the eastern end of the lake, where the impact of lake breezes is weaker. Gananoque subsequently shows less Doppler-shifting impact.

Negro Creek is another site within reasonable distance of a lakeshore, being about 40–50 km from at least two distinct shorelines to the west and north-east. This is approximately the inland distance to which lake breezes can typically have an impact (e.g., Miller *et al.*, 2003). Negro Creek shows some evidence of the same behaviour as Harrow and Walsingham at times, but not always; the effect is strongest in 2014–2017. Negro Creek also shows an interesting change in behaviour in the years 2013–2017 compared with 2008–2012. At this site, the lake breezes off Lake Huron and the upper synoptic flow are both from the west, so the helical structure and directional shear seen at Lake Erie are less likely: however, modest inter-annual changes in synoptic flow direction could significantly alter the development of shearing and subsequent IGW creation and Doppler shifting, so the changes may not be surprising. (It should also be noted here that there was a break in recording from September 2012 into early 2013, and it is tempting to believe that this may be associated with the change in apparent behaviour, perhaps due to an instrumental change? However, the radar was inactive due to a failed mother-board in the controlling computer; this was replaced with an identical motherboard while no other changes to the system were made, so the changes are real and not instrumental).

McGill (Montreal) is an interesting case. While it has no lake breezes of note, it does have some large rivers with associated topography (Ottawa River and St. Lawrence River), plus a complex of mountains in the surrounding area. The Appalachians to the south and east, Canadian Shield to the north and west, the St Lawrence Valley and the Ottawa River Valley all tend to channel winds in

preferred directions. (In this regard, Figure 2a is a little misleading: while the direct line of travel from Harrow to Montreal is somewhat flat, the region to the North of Montreal is quite hilly/mountainous and is better described by Figure 2b in the region closer to Aumond.) When these local low-altitude flows exist underneath synoptic-scale flows (the latter being produced by larger weather systems), waves generated in the lower levels may experience significant Doppler shifting on moving into the synoptic flow above. It is important throughout these considerations to recall that these plots are not necessarily about the intensity of the waves, but rather about the degree of Doppler shifting, since that is what distinguishes waves from turbulence.

Aumond shows some upper-tropospheric activity, but only modest Doppler shifting effects. However, some red is present, suggesting modest amounts of Doppler shifting: this may not be a complete surprise as the area is modestly hilly. Wilberforce, Markstay, Egbert and Abitibi Canyon show even less Doppler shifting impact.

Eureka, in the Arctic, is close to sea water, but is mainly surrounded by fjords (Slide Fjord and Eureka Sound), and is over 100 km from open sea. The sea is frozen for much of the year. Local wave generation is therefore expected to be largely orographic in nature. Nevertheless, there seems to be frequent Doppler shifting below 5 km altitude at times, with considerable year to year variability. Summertime data show more serious effects, and 2019 seems to have been especially active.

Several sites show noticeable slope flattening at the upper heights, around the tropopause, especially Eureka, Aumond, McGill, Gananoque and Harrow: an increase in wave effects at the troposphere would not be surprising, and would be consistent with these observations.

Here some of the important features that stand out in the graphs have been discussed; more detailed considerations will be dealt with in Section 7.

### 6.3 | Variability of spectral slopes

An important way to look at the waves versus 2-D turbulence argument is by using probability density functions (PDFs) of distributions of the slopes. Figure 8 shows PDFs of the slopes for the Egbert site and for Harrow. Both graphs show generally Gaussian shapes. However, there is clearly a difference in the means. The means, standard deviations and number of slopes used in each case for each site are (−2.054, 0.224, 1,189) and (−1.529, 0.271, 472) respectively. Evaluating the test statistic  $Z$  for a normal fit using the pooled standard errors gives a value of  $Z$  of 40.0, so the probability that these two graphs were derived from the same underlying distribution is well



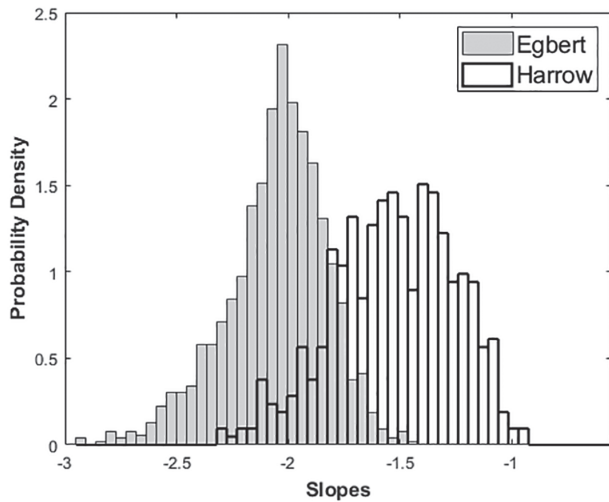


**FIGURE 8** PDFs of slopes for Egbert, and Wilberforce, 2010–2013. Months with occupancies less than 15% are excluded. The ordinate is probability per unit slope, and the area under each curve is unity

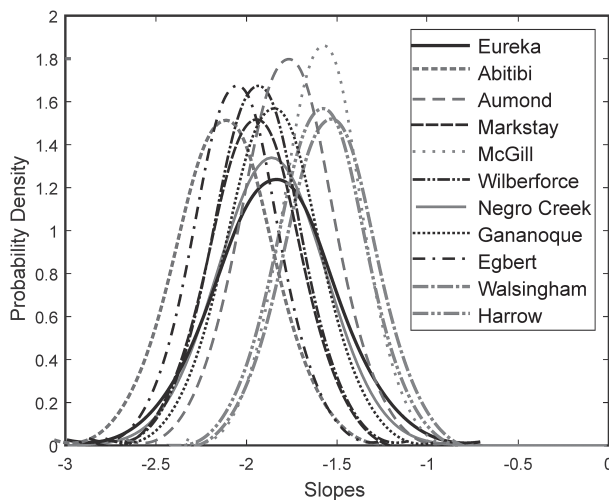


**FIGURE 9** Fitted Gaussians showing the PDFs of the slope distributions for each site. Areas under each curve are unity, so curves with greater width have smaller peak values. Data with occupancies in excess of 15% have been used. A colour version of this figure appears in the graphical abstract

below  $10^{-4}\%$ ; that is, the distributions are certainly statistically distinct.

Following the recognition that the Egbert and Harrow sites have statistically different mean slopes, PDFs for all sites were determined. These are shown in Figure 9, in this case using Gaussian fits to the PDFs to allow a cleaner presentation. All real PDFs are quite close to real Gaussians, as demonstrated in Figure 8, so use of Gaussians here is suitable.

As seen in Section 5.2.3, the errors due solely to the radar measurements are  $\sim \pm 0.1$  ( $\pm 0.2$  at the two-sigma

level), and when using averages, the errors for the mean will be even less (though not by  $\sqrt{N}$  times, since the central limit theorem cannot be used with regard to the radar measurement errors, whereas it can be used in limited form in regard to (somewhat uncorrelated) geophysical errors). The standard deviations of each of the spectra presented in Figure 9 substantially exceed our experimental error, so most of the spread is in fact geophysical. However, is the spread across the means of the different sites significant statistically?

As a partial answer to this question, an analysis of variance (ANOVA) has been performed on the data from the 11 sites. While the standard deviations of the sites do differ somewhat, the variation is less than  $\pm 20\%$ , which is close enough to warrant such a test.

The ANOVA produced the following clusters as having common means, with increasing values: (a) Abitibi (−2.11), (b) Egbert (−2.05), (c) Wilberforce and Markstay (−1.94), (d) Negro Creek, Gananoque and Eureka (−1.86), (e) Aumond (−1.74) and (f) McGill and Harrow (−1.58), and Walsingham (−1.54).

The conclusion is that the differences between sites are statistically real. The slopes vary over precisely the range of values suggested at the end of Section 4.2, with values as low as −2.5 (and even down to −3) being strongly suggestive of 2-D turbulence and values as high as −1 being indicative of strong Doppler shifting of IGWs.

Although our focus has been on the nominal north beam, the east beam was briefly analysed as well, as a check of the accuracy of the procedure. Both the IGW model and the 2-D turbulence model demonstrated in Figures 3 and 4 assume broad isotropy, so if this is true, results on the nominal “north” and “east” beams should be generally similar. A comparison between the north and east beams for Eureka (from 2015 to 2018 inclusive) is shown in the graphical abstract of this article, and general trends are similar, verifying the robustness of our work. Quantitatively, the cross-correlation coefficient between the two beams for Eureka over all years was 0.69, the range of N–E cross-correlation coefficients across all sites was from 0.44 to 0.88, while the mean across all sites was 0.69 with a standard deviation between sites of 0.15.

A larger comparison of north and east beams is presented in Appendix S3 (Figure S3.4). Detailed comparisons will be left to a later article.

### 6.4 | Retrospective examination of spectral linearity

At the end of the first paragraph of Section 5.2.1, it was mentioned that the general linearity of the spectra in the frequency band of interest would be revisited

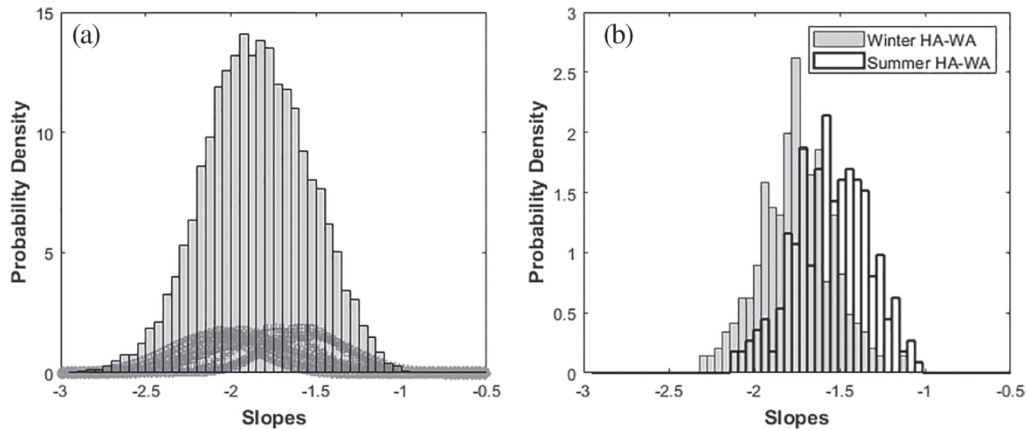


**FIGURE 10** (a) PDFs of slopes for all sites over all years. For reference, the Gaussian fits to PDFs for each of the sites individually are shown on the same scaling as the main graph (as taken from Figure 9). The area under each of the Gaussians is unity; the area under the larger histogram is set to 11 (sum of areas of all sites). (b) Combined PDFs of slopes for nominal summer and non-summer months from Harrow and Walsingham for altitudes between 2 and 4.5 km for all years

retrospectively. To this end, please refer to Appendix S3, at the end of which we carry out two tests. First, values of the lower cut-off frequency were chosen at (i)  $f_1/2$  then (ii)  $f_1$ , and height–time matrices of the slopes were produced for each cut-off. These were each then cross-correlated with the height–time matrices produced by the F–D selection, and the cross-correlation coefficients were 0.91 and 0.66, respectively, for the example displayed in S3. Other sites behaved similarly. Such good correlations between slopes determined using different bandwidths can only occur if the general behaviour across the band is approximately linear.

Secondly, quadratics were fitted to all spectra like Figure 5a,b. Samples are shown in S3. Significant deviations from linearity in our band of interest would produce noticeable curvature in these fits. Two different formats are presented, and it is seen there that, in a random sampling of data, individual quadratic plots are very linear in the critical band between  $\log_{10}(\text{frequency})$  of  $-5.1$  and  $-4.5$ . When looking at overall averages, the average quadratic plots are very linear between  $-5.4$  and  $-4.25$ . As discussed in S3, these numbers are all supportive of a quite recognizable linear portion of the spectrum which extends well to the left of  $f_1$ . The region we have called the “external wave region” is in fact filled with other waves and turbulence, and no “hole” appears here after Doppler shifting effects are considered.

## 6.5 | The overall picture

In Figure 10a, the distribution of slopes from all radars is plotted for data with occupancy above 15%. The overall PDF is a sum of these multiple individual graphs.

The mean for the combined graph is  $-1.847$ , the number of contributing slopes is 13,952, and the resulting standard deviation is 0.308. Taking the instrumental error as  $\sim 0.1$ , the geophysical standard deviation is  $\sqrt{(0.308^2 - 0.1^2)} = 0.291$ , so the geophysical variability well exceeds the measurement error.

Some additional features in Figure 7 deserve attention. The first is the tendency for many shallow slopes in summer (red colouring), even at the lowest heights. The second is a tendency for slopes as steep as  $-2.5$  in many of the contour maps, especially at heights below  $\sim 5$ – $8$  km. The third is a tendency (less discernible from Figure 7 but evident nevertheless), for the slopes in the non-summer months at 2–4.5 km altitude for all sites to be concentrated in the range of values from  $-1.5$  to  $-2$ . This can be seen somewhat more clearly in Figure 6, where a band of green/cyan colouring can be seen at 2–5 km at all three sites in the non-summer months (remember that a different colour palette is used in Figure 6 than in Figure 7).

These items will be further discussed in the “Discussion” section, but here some pertinent statistics will be summarized. First we consider summer and non-summer months.

The “summer” will be especially discussed in relation to convection, so the months from May to August will be included (tornadoes occur as early as April in southern Ontario, so the effects of convection are certainly evident by May). “Non-summer” months (loosely referred to as “winter”) will be considered as October to March inclusive. September and April are considered as transitional months and will be ignored.

Figure 10b shows PDFs of the slopes between 2.0 and 4.5 km altitude for Walsingham and Harrow (these being the cases with the shallowest slopes of all the sites) for

**TABLE 1** Mean slopes, standard deviations and numbers of contributing slopes for Harrow, Walsingham and McGill at 2–4.5 km altitude, as well as for all sites with and without Harrow, Walsingham and McGill

Sites → (2.0–4.5 km)	Harrow + Wals	Harrow + Wals + McGill	Non Harrow/ Wals.	Non-Harrow/ Wals/McGill	All sites included
Summer	–1.542	–1.536	–1.750	–1.785	–1.716
	0.227	0.198	0.251	0.245	0.258
	288	486	1,454	1,256	1,742
Non-summer	–1.735	–1.721	–1.944	–1.977	–1.909
	0.220	0.204	0.258	0.249	0.264
	354	562	1,763	1,555	2,117

both “summer” and “non-summer”. The two PDFs are distinctly offset from each other, and the means for the summer and non-summer (“winter”) months are –1.542 and –1.735, respectively. These are statistically different.

For comparison, PDFs of slopes for summer and non-summer months at 2–4.5 km altitude for all sites combined have been prepared, covering all years, and results are presented in Table 1. This shows means, standard deviations and numbers of slopes used for various combinations of sites and months. In particular, we examine the three most active sites (i.e., those showing greatest evidence of Doppler shifting effects, viz. Harrow, Walsingham and McGill), and consider these cases combined, all cases without these three sites and all sites collectively.

It is clear that, in all cases, the summer-time slopes exceed the non-summer values at 2–4.5 km altitude, with the three “active sites” having very flat slopes in summer (all close to –1.54). All standard deviations are ~0.20 to 0.25, somewhat less than the standard deviations for all heights, which are ~0.3. Hence there seems to be a general tendency for gravity waves to be more common in summer, since slopes are flatter then. This could be expected due to the increased convective activity expected at that time of year.

## 7 | DISCUSSION

### 7.1 | Distinctive low-level flows

McGill, Harrow and Walsingham all showed a tendency towards flatter (less negative) slopes over much of the year, but especially in summer. It was noted in Section 6.2 that each of these sites often have quite different flows at low and mid-altitudes, with flows at low levels influenced by orography (McGill) and lake breezes (Walsingham and Harrow), and flows at higher altitudes dominated by larger-scale synoptic flows. This set of circumstances can lead to gravity wave generation (through shearing

effects) with subsequent Doppler shifting as the waves move upward into the synoptic flow.

The activity at 7–11 km may also be related to the above effects. Waves generated by the shearing and localized convective processes discussed above may propagate upward and reach the tropopause, whereupon they may be reflected back down and create a standing wave which may amplify, leading to stronger gravity-wave oscillations than normal. In the presence of stronger upper-tropospheric winds, this may explain the flattening of the slopes here. This proposal is somewhat similar to the proposal by Peltier and Scinocca (1990), which used a similar “resonant standing wave” model to explain the production of the Chinook winds. Regardless of the mechanism of generation, our results suggest that IGWs, and associated Doppler shifting, are important contributors to the spectra at lake-side locations at mid to high tropospheric altitudes.

Another point is evident from Figure 7. This is the fact that, at the lowest altitudes (<2 km), the slopes are shallow (red in colour) at many sites. This region is close to the boundary layer, where dynamics can be quite different from the upper altitudes. The assumptions of statistical stationarity and homogeneity may break down here. Importantly, this will be a region dominated by convection, where vertical velocities can be relatively large, often considerably larger than those predicted by either 2-D turbulence (i.e., zero) or wave theory. The vertical winds will contribute significantly to our measured radial velocities, and since our spectra are determined assuming small vertical winds, the impact of unusually large vertical velocities at periods of a few hours may substantially flatten the curves. Frequent storms could also enhance the vertical winds. The most important parameter is not the vertical velocities per se, but the ratio of vertical velocities to horizontal velocities, which can be quite large at the lowest altitudes. Although contamination from strong convective vertical motions is a reasonable explanation for the flatter curves below 2 km, it is unproven at this time, and we

therefore choose not to formally interpret these results for the lowest 2 km.

## 7.2 | Final remarks

This study has focused on examination of slopes. Many other parameters can be measured, such as integrated spectral power. This has not been done here, since others have already demonstrated the large natural variability of mean square fluctuations (e.g., Nastrom and Gage, 1985; Nastrom *et al.*, 1987), but the proof that these effects were due to gravity waves and not 2-D turbulence, while significant, was not fully conclusive. Indeed, Nastrom and Gage (1985) initially ascribed their *k*-spectra as due to 2-D turbulence. We therefore looked for a more robust parameter, and used the O-QNet radar network to do this.

Future studies will use the other beams, and ways to integrate multiple beams will be investigated, to increase our data rates. It may be of value to also incorporate vertical beam data. Future studies may even include full vector treatments, but that may require refinement to the theory of FVZ87. Total spectral content will also be determined. Momentum flux measurements may also be of value. For now, however, this new tool will allow better studies of the relative effects of contributions of gravity waves and 2-D turbulence in the atmosphere.

## 8 | CONCLUSIONS

By measuring the geographic and temporal distribution of the slopes of  $\log_{10}$  power spectral densities versus  $\log_{10}$  frequency of radial wind components measured with wind profiler radars in Canada, it has been shown that the values of these slopes can be used to discriminate regions dominated by waves from regions dominated by 2-D turbulence. Steep negative slopes ( $< -2.1$ ) are strongly indicative of 2D turbulence, while shallow slopes of  $-1.5$  down to  $-1.0$  or so can only really be explained by a predominantly IGW-driven regime. Site-to-site variations are evident. Nevertheless, the loose similarity of sites physically separated by thousands of kilometres, such as lower Canada and the Arctic (Eureka), shows that a “quasi-universal” law does seem to apply (e.g., see Figure 9, where different sites show statistically different distributions, yet Eureka fits comfortably into the mix). Our results reinforce the idea that wind motions at temporal scales from 3–4 hrs to 15–20 hrs periodicity receive significant, and often dominant, contributions from Doppler-shifted buoyancy waves, especially in the upper troposphere and lower stratosphere, but that a significant background of 2-D turbulence exists. Lake breezes

seem to be a good example of wave generation with subsequent Doppler shifting, as shown by the sites at Harrow and Walsingham. The ability of waves to carry momentum and energy long distances makes them very different from 2-D turbulence, as waves generated at one location have the potential to affect events considerable distances away. Strong enhancements in spectral flattening around and above the tropopause (11–14 km) are evident for most radars, demonstrating that IGWs become increasingly significant as the stratosphere is approached. In some cases, seasonal effects are seen, such as summer–winter differences and annually repetitive patterns (Figure 6). At lower altitudes, especially between 2 and 5 km, 2-D turbulence appears to make a significant (often dominant) contribution to the spectra. The results below 2 km altitude require further analysis and interpretation.

An interesting side note of our studies arose in regard to the behaviour of spectra at very low frequencies, especially below  $10^{-5}$  Hz, around periods of 1–2 days and longer. The spectra at times become quite flat in this frequency region; this may be a quasi-instrumental effect due to a collapse of the Taylor frozen-in turbulence hypothesis, coupled with the natural decorrelation of weather system on time scales of days, as discussed towards the end of Section 4.2 and also in regard to Figure 5.

## ACKNOWLEDGEMENTS

We would like to acknowledge the support of the Canada Foundation for Innovation (CFI), which funded the radar network construction, as well as support from the Natural Sciences and Engineering Research Council of Canada (NSERC). Thanks also go to James Drummond and CAN-DAC (CANadian Network for the Detection of Atmospheric Change) for funding and supporting the installation at Eureka. We are also grateful to Prof. Isztar Zawadzki, who initiated the first windprofiler of the O-QNet by arranging its installation at McGill University. The efforts of Anna Hocking for her unflinching support throughout the lifetime of the O-QNet are also appreciated. Useful discussions with Rolando Garcia are also acknowledged.


## AUTHOR CONTRIBUTIONS

**Wayne Hocking:** Conceptualization; data curation; formal analysis; funding acquisition; investigation; methodology; project administration; resources; software; supervision; validation; visualization; writing – original draft; writing – review and editing. **Sergio Dempsey:** Investigation; methodology; software; validation; visualization; writing – review and editing. **Mel Wright:** Formal analysis; investigation; software; validation;



writing – review and editing. **Peter Taylor:** Funding acquisition; investigation; project administration; supervision; validation; writing – review and editing. **Frederic Fabry:** Investigation; methodology; validation; writing – review and editing.

## ORCID

Wayne K. Hocking  <https://orcid.org/0000-0003-0111-8804>

## REFERENCES

- Alexander, L., Sills, D. and Taylor, P. (2018) Initiation of convective storms at low-level mesoscale boundaries in southwestern Ontario. *Weather and Forecasting*, 33(4), 583–598.
- Bendat, J.S. and Piersol, A.G. (2000) *Random Data: Analysis and Measurement Procedures*. New York, NY: Wiley.
- Bühler, O., Callies, J. and Ferrari, R. (2014) Wave-vortex decomposition of one-dimensional ship-track data. *Journal of Fluid Mechanics*, 756, 1007–1026.
- Burrows, W.R., King, P., Lewis, P.J., Kochtubajda, B., Snyder, B. and Turcotte, V. (2002) Lightning occurrence patterns over Canada and adjacent United States from lightning detection network observations. *Atmosphere-Ocean*, 40(1), 59–80. <https://doi.org/10.3137/ao.400104>.
- Chang, E.K.M., Lee, S. and Swanson, K.L. (2002) Storm track dynamics. *Journal of Climate*, 15, 2163–2183. [https://doi.org/10.1175/1520-0442\(2002\)015<02163:STD>2.0.CO;2](https://doi.org/10.1175/1520-0442(2002)015<02163:STD>2.0.CO;2).
- Cheney, W. (2009) *Linear Algebra: Theory and Applications*. Sudbury, MA: Jones and Bartlett, p. 544, 558.
- Cho, J.Y. and Lindborg, E. (2001) Horizontal velocity structure functions in the upper troposphere and lower stratosphere. Part I. observations. *Journal of Geophysical Research*, 106(D10), 10223–10232.
- Eckermann, S.D. and Hocking, W.K. (1989) The effect of superposition on measurements of atmospheric gravity waves: a cautionary note and some re-interpretations. *Journal of Geophysical Research*, 94, 6333–6339.
- Ferraz-Mello, S. (1981) Estimation of periods from unequally spaced observations. *The Astronomical Journal*, 86(4), 619–624.
- Fritts, D.C. and Van Zandt, T.E. (1987) Effects of Doppler shifting on the frequency spectra of atmospheric gravity waves. *Journal of Geophysical Research*, 92(D8), 9723–9732.
- Fritts, D.C. and Alexander, M.J. (2003) Gravity wave dynamics and effects in the middle atmosphere. *Reviews of Geophysics*, 41, 1003. <https://doi.org/10.1029/2001RG000106>.
- Fritts, D.C., Smith, R.B., Taylor, M.J., Doyle, J., Eckermann, S.D., Dörnbrack, A., Rapp, M., Williams, B.P., Pautet, P.-D., Bossert, K., Criddle, N.R., Reynolds, C.A., Reinecke, P.A., Uddstrom, M., Revell, M.J., Turner, R., Kaifler, B., Wagner, J.S., Mixa, T., Kruse, C.G., Nugent, A.D., Watson, C.D., Gisinger, S., Smith, S.M., Lieberman, R.S., Laughman, B., Moore, J.J., Brown, W.O., Haggerty, J.A., Rockwell, A., Stossmeister, G.J., Williams, S.F., Hernandez, G., Murphy, D., Klekociuk, A.P., Reid, I.M. and Ma, J. (2016) The deep propagating gravity wave experiment (DEEPWAVE): an airborne and ground-based exploration of gravity wave propagation and effects from their sources throughout the lower and middle atmosphere. *Bulletin of the American Meteorological Society*, 97(3), 425–453. <https://doi.org/10.1175/BAMS-D-14-00269.1>.
- Gage, K.S. (1979) Evidence for a  $k^{-5/3}$  Law inertial range in mesoscale two dimensional turbulence. *Journal of the Atmospheric Sciences*, 36, 1950–1954.
- Gardner, C.S., Hostetler, C.A. and Franke, S.J. (1993) Gravity wave models for the horizontal wave number spectra of atmospheric velocity and density fluctuations. *Journal of Geophysical Research*, 98, 1035–1049. <https://doi.org/10.1029/92JD02051>.
- Geller, M.A., Alexander, M.J., Love, P.T., Bacmeister, J., Ern, M., Hertzog, A., Manzini, E., Preusse, P., Sato, K., Scaife, A.A. and Zhou, T. (2013) A comparison between gravity wave momentum fluxes in observations and climate models. *Journal of Climate*, 26(17), 6383–6405. <https://doi.org/10.1175/JCLI-D-12-00545.1>.
- Hastie, D.R., Narayan, J., Schiller, C., Niki, H., Shepson, P.B., Sills, D.M.L., Taylor, P.A., Moroz, W.J., Drummond, J.W., Reid, N., Taylor, R., Roussel, P.B. and Melo, O.T. (1999) Observational evidence for the impact of lake breeze circulation on ozone concentrations in southern Ontario. *Atmospheric Environment*, 33, 323–335.
- Hocking, W.K. (1997) System design, signal processing procedures and preliminary results for the Canadian (London, Ontario) VHF atmospheric radar. *Radio Science*, 32, 687–706.
- Hocking, W., Taylor, P., Swarnalingam, N., Argall, P.S., Tarasick, D., Zawadzki, I., Fabry, F., Barron, J., Mercer, R., Klaassen, G., McBean, G., Sica, R. and Hangan, H. (2009) Progress report on the O-QNET, a new Canadian windprofiler network. In: Swarnalingam, N. and Hocking, W.K. (Eds.) *Proceeding of the Twelfth International Workshop on Technical and Scientific Aspects of MST Radar*, May 17–23, 2009. London, ON: The Canadian Association of Physics, pp. 179–182.
- Hocking, W.K., Röttger, J., Palmer, R.D., Sato, T. and Chilson, P.B. (2016) *Atmospheric Radar: Application and Science of MST Radars in the Earth's Mesosphere, Stratosphere, Troposphere, and Weakly Ionized Regions*. Cambridge: Cambridge University Press, p. 2016. <https://doi.org/10.1017/9781316556115>.
- Hoskins, B.J. and Hodges, K.I. (2018) The annual cycle of northern hemisphere storm tracks. Part I: seasons. *Journal of Climate*, 32, 1743–1760. <https://doi.org/10.1175/JCLI-D-17-0870.1>.
- Illingworth, A.J., Cimini, D., Gaffard, C., Haeffelin, M., Lehmann, V., Löhnert, U., O'Connor, E.J. and Ruffieux, D. (2015) Exploiting existing ground-based remote sensing networks to improve high-resolution weather forecasts. *Bulletin of the American Meteorological Society*, 96, 2107–2125. <https://doi.org/10.1175/BAMS-D-13-00283.1>.
- King, P., Sills, D., Hudak, D., Joe, P., Donaldson, N., Taylor, P., Qiu, X., Rodriguez, P., Leduc, M., Synergy, R. and Stalker, P. (1999) ELBOW: an experiment to study the effects of Lake breezes on weather in southern Ontario. *CMOS Bulletin*, 27, 35–41.
- King, P.W.S., Leduc, M.J., Sills, D.M.L., Donaldson, N.R., Hudak, D.R., Joe, P. and Murphy, B.P. (2003) Lake breezes in southern Ontario and their relation to tornado climatology. *Weather and Forecasting*, 18, 795–807.
- Koshyk, J.N. and Hamilton, K. (2001) The horizontal kinetic energy spectrum and spectral budget simulated by a high-resolution troposphere-stratosphere-mesosphere GCM. *Journal of the Atmospheric Sciences*, 58, 329–348.
- Lilly, D.K. (1983) Stratified turbulence and the mesoscale variability of the atmosphere. *Journal of the Atmospheric Sciences*, 40, 749–761.
- Lilly, D.K. (1989) Two-dimensional turbulence generated by energy-sources at 2 scales. *Journal of the Atmospheric Sciences*, 46, 2026–2030.

- Lin, C.C. (1953) On Taylor's hypothesis and the acceleration terms in the Navier–Stokes equation. *Quarterly of Applied Mathematics*, 10, 295–306. <https://doi.org/10.1090/qam/51649>.
- Lindborg, E. (1999) Can the atmospheric kinetic energy spectrum be explained by two-dimensional turbulence? *Journal of Fluid Mechanics*, 388, 259–288.
- Lindzen, R.S. (1981) Turbulence and stress owing to gravity wave and tidal breakdown. *Journal of Geophysical Research*, 86, 9707–9714.
- Lumley, J.L. (1965) Interpretation of time spectra measured in high-intensity shear flows. *The Physics of Fluids*, 8, 1056. <https://doi.org/10.1063/1.1761355>.
- Marengo, A., Thouret, V., Nedelec, P., Smith, H., Helten, M., Kley, D., Karcher, F., Simon, P., Law, K., Pyle, J., Poschmann, G., Von Wrede, R., Hume, C. and Cook, T. (1998) Measurement of ozone and water vapor by airbus in-service aircraft: the MOZIC airborne program, an overview. *Journal of Geophysical Research – Atmospheres*, 103, 25631–25642.
- Mariani, Z., Dehghan, A., Joe, P. and Sills, D. (2018) Observations of lake-breeze events during the Toronto 2015 Pan-American Games. *Boundary-Layer Meteorology*, 166, 113–135. <https://doi.org/10.1007/s10546-017-0289-3>.
- Miller, S.T.K., Keim, B.D., Talbot, R.W. and Mao, H. (2003) Sea breeze: structure, forecasting, and impacts. *Reviews of Geophysics*, 41(3), 1011.
- Minamihara, Y., Sato, K., Tsutsumi, M. and Sato, T. (2018) Statistical characteristics of gravity waves with near-inertial frequencies in the Antarctic troposphere and lower stratosphere observed by the PANSY radar. *JGR Atmospheres*, 123(17), 8993–9010.
- Nastrom, G.D. and Gage, K.S. (1985) A climatology of atmospheric wavenumber spectra of wind and temperature. *Journal of the Atmospheric Sciences*, 42, 950–960.
- Nastrom, G.D., Fritts, D.C. and Gage, K.S. (1987) An investigation of terrain effects on the mesoscale spectrum of atmospheric motions. *Journal of the Atmospheric Sciences*, 44, 3087–3096.
- Peltier, W.R. and Scinocca, J.F. (1990) The origin of severe down-slope windstorm pulsations. *Journal of the Atmospheric Sciences*, 47, 2853–2870.
- Piani, C., Durran, D., Alexander, M.J. and Holton, J.R. (2000) A numerical study of three-dimensional gravity waves triggered by deep tropical convection and their role in the dynamics of the QBO. *Journal of the Atmospheric Sciences*, 57, 3689–3702.
- Pisoff, P., Sacha, P., Miksovsky, J., Haszar, P., Scherllin-Pirscher, B. and Foelsche, U. (2018) Revisiting internal gravity waves analysis using GPS RO density profiles: comparison with temperature profiles and application for wave field stability study. *Atmospheric Measurement Techniques*, 11, 515–527. <https://doi.org/10.5194/amt-11-515-2018>.
- Scheffler, A.O. and Liu, C.H. (1985) On observation of gravity wave spectra in the atmosphere by using MST radars. *Radio Science*, 20, 1309–1322.
- Scheffler, A.O. and Liu, C.H. (1986) The effects of Doppler shift on the gravity wave spectra observed by MST radar. *Journal of Atmospheric and Terrestrial Physics*, 48, 1225–1231.
- Sills, D.M.L., Brook, J.R., Levy, I., Makar, P.A., Zhang, J. and Taylor, P.A. (2011) Lake breezes in the southern Great Lakes region and their influence during BAQS-met 2007. *Atmospheric Chemistry and Physics*, 11, 7955–7973. <https://doi.org/10.5194/acp-11-7955-2011>.
- Smith, S.A., Fritts, D.C. and Van Zandt, T.E. (1985) Comparison of mesospheric wind spectra with a gravity wave model. *Radio Science*, 20, 1331–1338.
- Smith, S.A., Fritts, D.C. and Van Zandt, T.E. (1987) Evidence for a saturated spectrum of gravity waves. *Journal of the Atmospheric Sciences*, 44, 1404–1410.
- Sutherland, B. (2010) *Internal Gravity Waves*. Cambridge: Cambridge University Press. <https://doi.org/10.1017/CBO9780511780318>.
- Taylor, P.A., Weng, W., Wang, Z.Q., Corkum, M., Malik, K., Sharma, S. and Hocking, W. (2016) Upper-level winds over southern Ontario: O-QNet wind profiler and NARR comparisons. *Atmosphere-Ocean*, 55(1), 1–11. <https://doi.org/10.1080/07055900.2016.1231658>.
- Taylor, G.I. (1938) The spectrum of turbulence. *Proceedings of the Royal Society A*, A132, 476–490.
- Thayaparan, T., Hocking, W.K. and MacDougall, J. (1995) Observational evidence of tidal/gravity wave interactions using the UWO 2 MHz radar. *Geophysical Research Letters*, 22, 373–376.
- Tung, K.K. and Orlando, W.W. (2003) The  $k^{-3}$  and  $k^{-5/3}$  energy spectrum of atmospheric turbulence: Quasigeostrophic two-level model simulation. *Journal of the Atmospheric Sciences*, 60, 824–835.
- Van Zandt, T.E. (1985) A model for gravity wave spectra observed by Doppler sounding systems. *Radio Science*, 20, 1323–1330.
- Walterscheid, R.L. and Hocking, W.K. (1991) Stokes diffusion by atmospheric internal gravity waves. *Journal of the Atmospheric Sciences*, 48, 2213–2230.
- Wright, M.C. (2014) *Gravity wave spectra morphology in the Arctic and non-Arctic lower atmosphere*. MSc Thesis, Department of Physics and Astronomy, University of Western Ontario, London, ON.
- Wyngaard, J.C. and Clifford, S.F. (1977) Taylor's hypothesis and high-frequency turbulence spectra. *Journal of the Atmospheric Sciences*, 34, 922–929.

## SUPPORTING INFORMATION

Additional supporting information may be found online in the Supporting Information section at the end of this article.

**How to cite this article:** Hocking, W.K., Dempsey, S., Wright, M., Taylor, P. & Fabry, F. (2021) Studies of relative contributions of internal gravity waves and 2-D turbulence to tropospheric and lower-stratospheric temporal wind spectra measured by a network of VHF windprofiler radars using a decade-long data set in Canada. *Quarterly Journal of the Royal Meteorological Society*, 147(740), 3735–3758. Available from: <https://doi.org/10.1002/qj.4152>

## APPENDIX A: MODELLING THE SIGNAL

To verify the accuracy of our data and better interpret them, a spectral model of wave motions in the atmosphere

was developed. While empirical analytic models are available for this purpose, such as Van Zandt (1985), FVZ87 and Gardner *et al.* (1993) (among others), such average spectral representations are inadequate. To properly represent our data, phase variations, and the fact that waves often come in packets, needed to be incorporated. Therefore the approach used in Walterscheid and Hocking (1991) was applied to develop a realistic spectrum, including the effects of phase variations. This procedure is explained below.

An example of a realistic spectrum from the Eureka site is shown in Figure A1a. For the model, a collection of waves with different periods and horizontal wavelengths was assembled (for an example, see Table S4.1 in Appendix S4), where the amplitudes followed a spectral form similar to that of Walterscheid and Hocking (1991). Our intent was to find spectra similar in some detail to Figure A1a. Vertical wavelengths have been calculated using the gravity wave dispersion relations presented by Walterscheid and Hocking (1991), equation (43) (also see the main text of this article, Equation (4)). These are quite general and describe non-hydrostatic compressible flow on an  $f$ -plane with Rayleigh drag. Amplitudes have then been ascribed according to the spectral laws shown in the above-mentioned articles, and random phases have been ascribed to each of these waves. The periods cover values associated with the Brunt-Väisälä oscillations to inertial-scale oscillations (and even slightly into the external-wave and planetary-wave domains), and horizontal wavenumbers from a few tens of kilometres up to several thousand kilometres have been used. Walterscheid and Hocking (1991) used 21 waves, which was adequate for their work on Stokes diffusion, but here 38 waves were needed for a reasonable representation. Once the velocity amplitudes were found, each wave was represented as  $v(t) = A(k, m, \omega) \times \exp\{i(kx + mz - \omega t + \phi)\}$ , then all the waves were added together for a chosen  $(x, z)$  coordinate, giving the complex velocity field as a function of time. From this, the spectrum is found.

To make the spectra even more realistic, the waves were not represented as continuous waves, but made into the form of wave packets, with envelopes varying from a few wavelengths to many tens of wavelengths. The waves were turned on and off using growth and decay functions that took the form of a cosine structure covering one half of a period of some suitably chosen growth/decay time  $T_G$ . The growth followed a formula as a function of time step  $j$  of the form  $A_G = 0.5 [-\cos(2\pi j/2T) + 1]$ , evaluated from  $j = 0$  to  $j = T$ , after which it stayed fixed at  $A_G = 1.0$ . Hence it grew smoothly from 0 to 1.0. The product of the growth term and the sinusoidal wave term was then used as the start of the wave packet. Likewise, a smooth decay was added at the end, of the form  $A_D = 0.5[\cos(2\pi[j - T_{\text{delay}}]/2T_D) + 1]$ ,

where  $T_D$  is the time over which the decay occurs, and  $T_{\text{delay}}$  is the time from the start at which the decay starts.

Thus, the amplitudes grew from zero amplitude to some peak value, then remained constant, and then decayed. Growth periods for the envelope were generally much longer than for the periods of the waves themselves, and less than the duration of the steady-state portion of the wave. Other forms of modulation were tried such as exponential decays, but in general the functional forms in the growth and decay phases were not of great consequence; the duration was more important. The key purpose was to smear the spectra out so as to produce a relatively smooth average spectrum (plus noise) with no particularly dominant peaks. The use of modulation in this way also represents realistic behaviour, since waves in the real atmosphere have finite lifetimes. This combination of wave packets with randomly chosen growth and decay times, random start times and random phases represented our real data in an excellent way.

The phases were randomized on each run, and the amplitudes followed the universal gravity wave spectrum. The parameters used in Table S4.1 led to a slope of approximately  $-1.4$ . Adjustments to the wave amplitudes could be made to achieve other slopes, such as  $-5/3$ . The results for a  $-5/3$  law are seen in Figure A1b, and are quite typical.

Figure A1b shows that the artificial spectrum generated in this way compares well visually with a real spectrum. It may be noted that modest spectral peaks can be seen in figure (b) at  $\log_{10}(\text{frequency}) = -4.5$  and  $-4.2$  rad  $s^{-1}$ , which might be considered as incorrect. However, they are in fact suitable. Modest dominant spectral lines like this also occurred in real spectra, and the model spectra also showed no such lines on other occasions. Many different spectral representation had small peaks, just as real-life applications show similar behaviour. In real life, this is largely due to statistical variations, and fortuitous effects related to the random selection of phases, which can lead to artificial occurrence of wave peaks. Such fortuitous summations can be deceptive, but are quite real, as discussed by Eckermann and Hocking (1989).

Note that no Doppler shifting was included in our model. This could be done, but was not the purpose here. While we have tried to keep the model quite general, its main purpose here was to determine the magnitudes of systematic and random errors in our fitting, nothing more. This also allows the same model to be used to represent 2-D turbulence, a point that will be discussed shortly.

Once the spectra had been developed in a theoretical way, it was possible to test the model. Data could be chosen at time steps matching real analyses, including allowing missing data points, adding some level of error in each “data point” measurement and adding some level

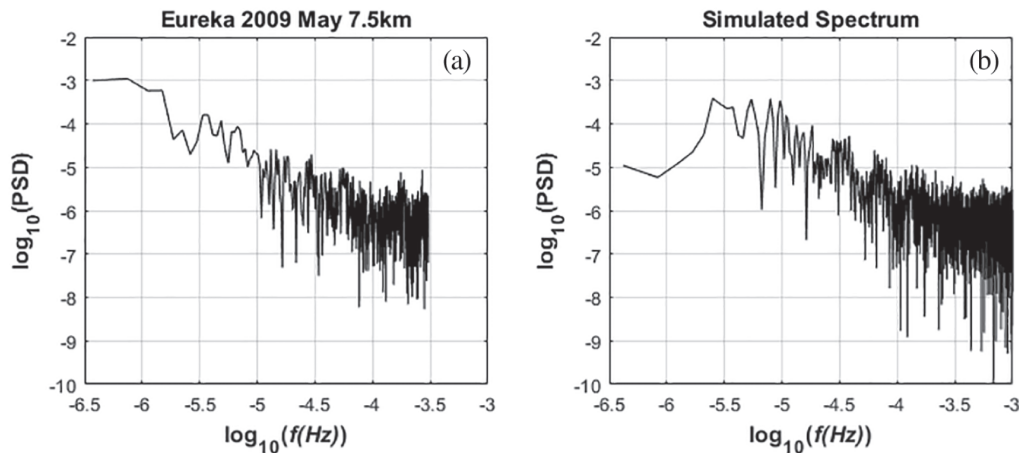


**FIGURE A1** Representative real and simulated power spectral densities: (a) a real-life spectrum determined from the Eureka radar and (b) a simulated spectrum determined using the procedure discussed in the text. Note that the units of frequency are Hz. The inertial frequency is at  $\log_{10}(f[\text{Hz}]) = -4.8$ . A value of  $\log_{10}(\text{frequency in Hz})$  equal to  $-4.0$  (where the signal starts to become higher than the noise to the left, and the noise to the right of this point is relatively flat in [a]) corresponds to a period of 10,000 s or about 2.7 hrs. This matches the right-hand edge of the grey region shown in Figure 3. The exact transition point (or “break-point”) between the wave spectrum and the noise varies from data set to data set, but is typically around this point. The method used to determine the true break-point is discussed in more detail in the main body of the text

of randomness to our sampling times. Periods of extended data loss could also be simulated. Simulations were performed using DCDF, just as for the real data.

Note that, while this spectral approach is based on waves, it is equally valid for representation of 2-D turbulence. The primary purpose is to use the model to determine any systematic and random errors in the slopes for *any* spectrum, regardless of its physical cause. While vertical wavelengths are included in the model, at any one given height the  $mz$  term in  $\exp\{i(kx + mz - \omega t + \phi)\}$  is really just a number, and can be simply considered as an extra phase term. So the representation is just a random sum

of weighted  $\exp\{i(kx - \omega t + \psi)\}$  terms, where  $\psi$  is a new random phase. Furthermore, our simulations were done at fixed  $(x, z)$ , so even the  $kx$  term is another constant for each wave, and  $\exp\{i(kx + mz - \omega t + \phi)\}$  can be written as  $\exp\{i(-\omega t + \psi_2)\}$ , where  $\psi_2$  is another random phase term. Both  $x$  and  $z$  can be chosen as zero if desired. Spectra from two-dimensional turbulence could equally be represented in this way, except in that case the ratio  $\omega/k$  would be simply the mean velocity of drift of the turbulence rather than a wave phase speed. In the end, both waves and 2-D turbulence can be suitably modelled in this way, and would have the same statistical characteristics.